energies

Article

Evaluation of Ground Motion Amplification Effects in Slope Topography Induced by the Arbitrary Directions of Seismic Waves

Chao Yin [1,*], Wei-Hua Li [2] and Wei Wang [3]

[1] State Key Laboratory of Mechanical Behavior and System Safety of Traffic Engineering Structures, Shijiazhuang Tiedao University, Shijiazhuang 050043, China
[2] School of Civil Engineering, Beijing Jiaotong University, Beijing 100044, China; whli@bjtu.edu.cn
[3] Key Laboratory of Roads and Railway Engineering Safety Control of Ministry of Education, Shijiazhuang Tiedao University, Shijiazhuang 050043, China; wangweiuuu@163.com
* Correspondence: robinyc@stdu.edu.cn; Tel.: +86-311-8793-9232

Abstract: The incident directions of seismic waves can change the ground motions of slope topography. To elaborate on the influences of the directions of seismic waves, a dynamic analysis of the slope topography was performed. Seismic waves were input using an equivalent nodal force method combined with a viscous-spring artificial boundary. The amplification of ground motions in double-faced slope topographies was discussed by varying the angles of incidence. Meanwhile, the components of seismic waves (P waves and SV waves), slope materials and slope geometries were all investigated with various incident earthquake waves. The results indicated that the pattern of the amplification of SV waves was stronger than that of P waves in the slope topography, especially in the greater incident angels of the incident waves. Soft materials intensely aggravate the acceleration amplification, and more scattered waves are produced under oblique incident earthquake waves. The variations in the acceleration amplification ratios on the slope crest were much more complicated at oblique incident waves, and the ground motions were underestimated by considering only the vertical incident waves. Therefore, in the evaluation of ground motion amplification of the slope topography, it is extremely important to consider the direction of incident waves.

Keywords: directions of incident waves; slope topography; amplification effects; ground motions; equivalent nodal forces

Citation: Yin, C.; Li, W.-H.; Wang, W. Evaluation of Ground Motion Amplification Effects in Slope Topography Induced by the Arbitrary Directions of Seismic Waves. *Energies* **2021**, *14*, 6744. https://doi.org/10.3390/en14206744

Academic Editor: Manoj Khandelwal

Received: 20 August 2021
Accepted: 13 October 2021
Published: 16 October 2021

1. Introduction

Earthquake-induced landslides are among the most hazardous secondary effects of strong seismicity in mountainous regions. Several historical cases highlight the potentially devastating consequences in the last 30 years [1–6] because nearly one-third of deaths are caused by earthquake-induced landslides among all disasters [7–10]. Many researchers have indicated that topographic effects have possible interactions between landslide mechanisms and triggering conditions [11–16]. Thus, the topographic effects, represented by the ground motions on the slope model, should be better understood.

Generally, convex topographies such as mountains, slopes and individual ridges lead to intense aggravation of the seismic responses irregularly along the ground surface [17]. Many acceleration-time histories recorded by the seismometers near the epicenter all proved that the peak acceleration at the slope crest showed intense amplification based on instrumental data from strong earthquakes such as the 1987 California earthquake, the 1994 Northridge earthquake, the 1995 Egion earthquake and the 2008 Wenchuan earthquake [12,18–20]. In addition, statistical analysis of the seismological stations in Iran and Israel showed that the acceleration amplification ratios with respect to the slope crest and ground could reach as much as four times [21,22]. These measured records confirmed that the slope topography modified the seismic ground motions.

In the analysis of topographic effects, both analytical and numerical methods were utilized [23–34]. Nevertheless, the analytical method (e.g., Newmark's method) can neither quantify the plastic strains of the non-shearing models nor consider the interaction between the models and the seismic waves in terms of ground motion amplification or de-amplification owing to irregular topographic patterns [17]. Conversely, the complicated stress-strain relationships can be described clearly based on the numerical method, and the expected plastic strain effects of the model can be quantified owing to seismic events [35]. Thus, for convex topographies (mountains, slopes and individual ridges), the most common method is a numerical simulation, such as finite difference methods [13,36–39], finite element methods [40–45], boundary element methods [37,46,47], generalized consistent transmitting boundary methods [29,30] and distinct element methods [48].

Many researchers have analyzed the ground motions in slope topography [13,36,37,40–45,49,50]; however, they preferred the vertical directions of incident waves rather than considering the influences of the incident angles. According to the regression analysis of numerous seismological records in America and Japan, the incident angles near the ground are usually oblique [51,52]. Undoubtedly, the oblique incident directions change the seismic wave paths in the slope model, and the different seismic responses lead to the irregularly intense amplification of the ground motions and aggravation of the slope instability [11,30]. Thus, the varied angles of incident waves definitely influence the amplification of the slope topography, and overlooking the wave inclination oversimplifies the analyses of the seismic responses on the ground motions. Even though this problem has been discussed by some researchers [30,35], there has been little systematic analysis of the influences of the incident directions on the ground motions in slope topography, such as the impacts of slope materials and sizes under oblique angles of incident waves.

Based on the analyses above, this study aimed to investigate the impact of the incident directions of seismic waves on the ground motions in slope topography. The remainder of this paper is organized as follows. The problem is proposed and the slope model is established in Section 2. The derivation of the input method in the numerical simulation with arbitrary directions of incident waves is presented in Section 3. In Section 4, the influencing factors (wave patterns, slope materials and slope geometries) are discussed separately under a double-faced slope topography with varying angles of incident waves. Finally, the conclusions and future prospects are presented in Section 5.

2. Problem Layout and Model Establishment

Topography has an important influence on the amplification of ground motions. The convex topography, which includes slopes, individual hills and mountains, leads to irregular amplification of the topographic effects. In this study, the configurations of the slopes, hills and mountains were simplified as double-faced slope topographies, and the universality of the inclinations of seismic waves that enter the site was considered. The impacts of the topographic effects were analyzed based on the double-faced slope topographies and the site effects were investigated under arbitrary directions of incident waves with other factors (e.g., components of the seismic waves, slope materials and slope sizes).

A dynamic finite element method (FEM) was used to analyze the ground motion process. Even though a three-dimensional (3-D) model was required to fully describe the topographic effects, two-dimensional (2-D) topographic profiles adequately captured the essential geometry of mountain ridges and allowed exploration of key features of the observed landslide patterns [35]. Thus, a 2-D homogeneous double-faced slope with varying slope sizes was established, as illustrated in Figure 1. The height of the slope was assumed to be H, which varied according to the wavelength λ. That is, the height of the slope was considered to be the normalized height in this study [36]. The width of the slope crest, W, corresponded to the slope height. The inclination of slope i evolved from gentle to steep. Moreover, the widths of the ground surfaces were 200 m per side, and the depths of the foundation were 200 m. The seismic waves were input from the left bottom of the

foundation with incident angles θ in the range of 0°–30°, with intervals of 5°. To ensure the accurate representation of wave transmissions through a model in the FEM, the element size of the model had to be less than one-twelfth of the wavelength [53], and the time step of the dynamic analysis was determined to be one-tenth of the maximum frequency of the seismic waves [13].

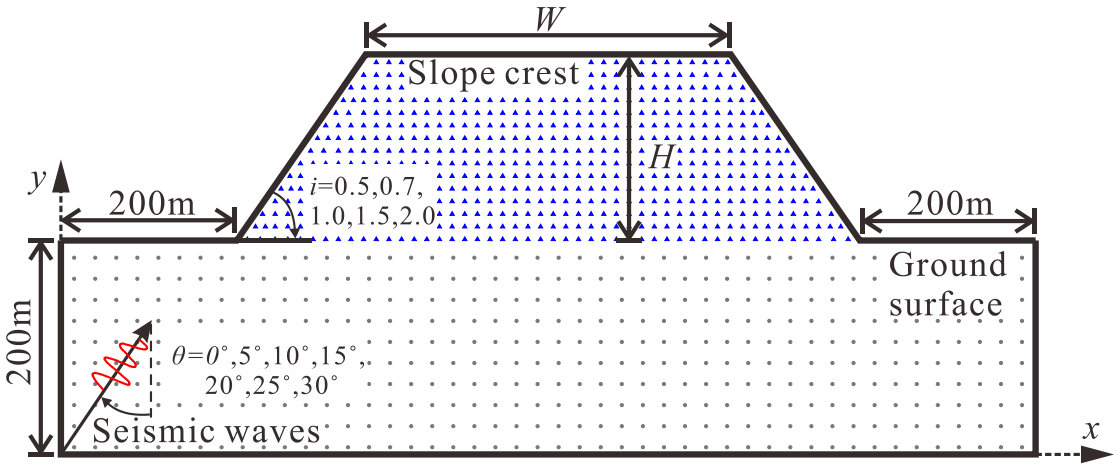

Figure 1. Sketch of the calculated modeling.

The seismic waves were analyzed by two components of the seismic waves (considering only the body waves), that is, P waves and SV waves. The influence of the wave components was analyzed using the same model size. The materials of the slope were assumed to be isotropic, and the medium was linearly elastic. To investigate the influence of materials in the evaluation of the topographic effects, the material of the foundation was fixed, whereas the materials of the slope varied according to the variations in the materials in the foundations. The specific parameters of the materials are presented in Table 1.

Table 1. Parameters of soil medium implemented in FEM.

Soil Types	Mass Density ρ (kg/m^3)	Poison's Ratio v	Elastic Modulus E (MPa)	P Wave Velocity c_p (m/s)	S Wave Velocity c_s (m/s)
Foundation	2000	0.2	768	653.1	400
Slope I	2000	0.2	768	653.1	400
Slope II	2000	0.3	425	534.8	285.9
Slope III	2000	0.25	1370	906.4	523.4

3. Input of Seismic Waves in Numerical Simulation

3.1. Establishment of the Artificial Boundary and the Input Method

In a dynamic analysis of the numerical simulation, the study area is usually truncated from an infinite region with an artificial boundary used to absorb the scattered waves. In this study, a viscous-spring artificial boundary was adopted [54,55]. The elastic springs and dampers were established to implement the viscous-spring artificial boundary on the boundary nodes, as shown in Figure 2. The coefficients of the elastic spring (K) and damper (C) are defined as follows.

$$K_N = \frac{1}{1+A}\frac{\lambda+2G}{R}\cdot A_l,\ \ C_N = B\rho c_p \cdot A_l \tag{1}$$

$$K_T = \frac{1}{1+A}\frac{G}{R}\cdot A_l,\ \ C_T = B\rho c_s \cdot A_l \tag{2}$$

where A and B are the correction coefficients; the good values of the coefficients are 0.8 and 1.1, respectively [56]; ρ is the mass density; R is the distance from the wave source to the boundary; c_p and c_s are the velocities of the compression wave and shear wave in the medium, respectively; G is the shear modulus; and subscripts T and N indicate the tangential and normal directions, respectively. A_l represents the influence area at each node, for example, at node l, $A_l = (A_1 + A_2)/2$, as depicted in Figure 2.

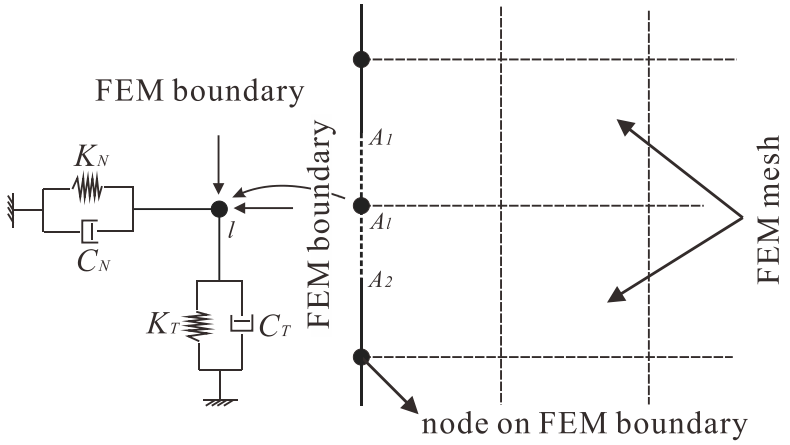

Figure 2. Layout of viscous-spring artificial boundary on FEM model.

The motion equation of the lumped mass in the FEM wavefield at the artificial boundary is expressed as follows:

$$m\ddot{\mathbf{u}} + c\dot{\mathbf{u}} + k\mathbf{u} = A\boldsymbol{\sigma} \tag{3}$$

In case of the distribution of the wavefield on the artificial boundary, the displacement and stress on the artificial boundary can be divided into free-field motions (denoted by superscripts f) and scattered-field motions denoted by superscripts s), which are illustrated as follows:

$$\mathbf{u} = \mathbf{u}^f + \mathbf{u}^s \boldsymbol{\sigma} = \boldsymbol{\sigma}^f + \boldsymbol{\sigma}^s \tag{4}$$

The equation of stress (specifically for the scattered-field motions) on the viscous-spring artificial boundary is given as:

$$\boldsymbol{\sigma}^s = -K\mathbf{u}^s - C\dot{\mathbf{u}}^s \tag{5}$$

Substituting Equations (4) and (5) into Equation (3), the motion equation on the artificial boundary is expressed as follows:

$$m\ddot{\mathbf{u}} + (c + AC)\dot{\mathbf{u}} + (k + AK)\mathbf{u} = A\boldsymbol{\sigma} + K\mathbf{u}^f + C\dot{\mathbf{u}}^f \tag{6}$$

Equation (6) can be considered seismic input and non-radiation, and the right side of the equation represents the equivalent nodal forces. When the two directions of the viscous-spring artificial boundary (normal direction and tangential direction) are considered, the equivalent nodal force can be expressed as follows:

$$\mathbf{f}_{li} = K_{li}\mathbf{u}_{li}^f + C_{li}\dot{\mathbf{u}}_{li}^f + A_l\boldsymbol{\sigma}_{li}^f \tag{7}$$

where subscript i denotes the direction and subscript l denotes the node. K_{li} and C_{li} are the coefficients of the elastic spring and damper, which can be calculated using Equations (1) and (2), respectively; $\boldsymbol{\sigma}_{li}^f$, $\mathbf{u}_{li}^f$ and $\dot{\mathbf{u}}_{li}^f$ represent the tensors of the stress, displacement and velocity, respectively.

3.2. Implementation of Oblique Incident Waves

3.2.1. SV Waves

Based on the artificial boundary, the other key point in the numerical simulation of a dynamic problem is the implementation of seismic waves in finite element models. An efficient and high-precision method is to convert the seismic records, that is, acceleration records, together with the coefficients of the artificial boundary into equivalent nodal forces. Figure 3 presents a plane study area that was subjected to oblique incident SV waves. As shown in Figure 3, each truncated boundary was subjected to three waves that involved one incident wave and two reflected waves. When node A, one of the joints on the left truncated boundary, were considered, the incident seismic waves of node A reached the boundary directly (incident SV waves) or through reflection after first reaching the ground surface (reflected SV waves and reflected P waves). The displacement and velocity of the incident SV waves are denoted as $u_s(t)$ and$\dot{u}_s(t)$, respectively.

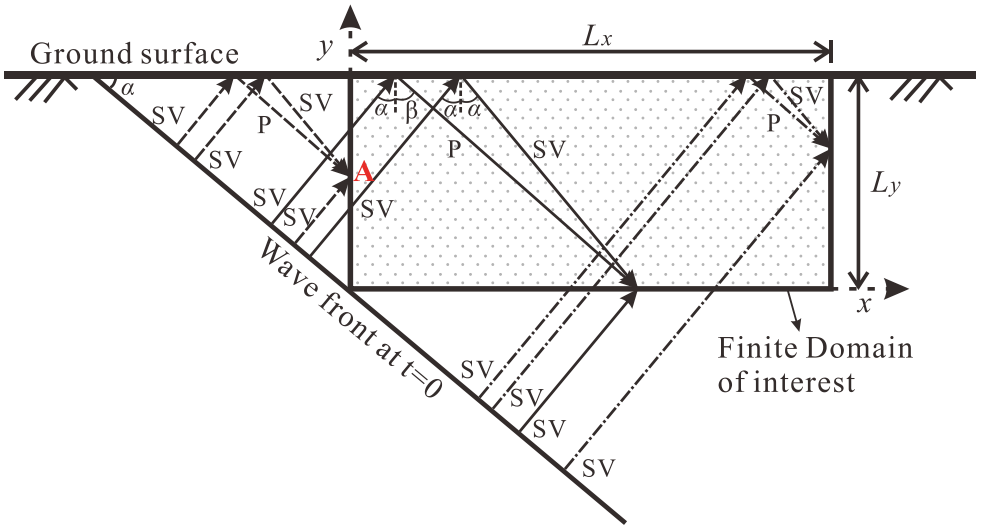

Figure 3. Sketch of the seismic waves on truncated boundary by obliquely incident SV waves.

Consequently, the free-field motion and the associated stress (in terms of x and y components) can be induced at the given point A (x_0, y_0) as follows:

$$\begin{cases} u_{lx}(t) = u_s(t-\Delta t_1)\cos(\alpha) - A_1 u_s(t-\Delta t_2)\cos(\alpha) + A_2 u_p(t-\Delta t_3)\sin(\beta) \\ u_{ly}(t) = -u_s(t-\Delta t_1)\sin(\alpha) - A_1 u_s(t-\Delta t_2)\sin(\alpha) + A_2 u_p(t-\Delta t_3)\cos(\beta) \\ \dot{u}_{lx}(t) = \dot{u}_s(t-\Delta t_1)\cos(\alpha) - A_1 \dot{u}_s(t-\Delta t_2)\cos(\alpha) + A_2 \dot{u}_p(t-\Delta t_3)\sin(\beta) \\ \dot{u}_{ly}(t) = -\dot{u}_s(t-\Delta t_1)\sin(\alpha) - A_1 \dot{u}_s(t-\Delta t_2)\sin(\alpha) + A_2 \dot{u}_p(t-\Delta t_3)\cos(\beta) \end{cases} \tag{8}$$

$$\begin{cases} \sigma_{lx} = S_1\left(\dot{u}_s(t-\Delta t_1) + S_2 A_1 \dot{u}_s(t-\Delta t_2)\right) + S_3 A_2 \dot{u}_p(t-\Delta t_3) \\ \sigma_{ly} = S_4\left(\dot{u}_s(t-\Delta t_1) + S_5 A_1 \dot{u}_s(t-\Delta t_2)\right) + S_6 A_2 \dot{u}_p(t-\Delta t_3) \end{cases} \tag{9}$$

where A_1 and A_2 are the amplitude ratios (denoted as the reflected SV waves and reflected P waves to the incident SV waves), Δt is the delay time of waves from the wavefront at $t = 0$ to the boundary node (node A), α and β are the angles between the vertical direction and reflected SV waves, and the reflected P waves, respectively. A_1, A_2 and β can be expressed as follows:

$$\begin{cases} A_1 = \frac{{c_s}^2 \sin 2\alpha \sin 2\beta - {c_p}^2 \cos^2 2\alpha}{{c_s}^2 \sin 2\alpha \sin 2\beta + {c_p}^2 \cos^2 2\alpha} \\ A_2 = \frac{2 c_p c_s \sin 2\alpha \cos 2\alpha}{{c_s}^2 \sin 2\alpha \sin 2\beta + {c_p}^2 \cos^2 2\alpha} \\ \beta = \arcsin\left(\frac{c_p \sin\alpha}{c_s}\right) \end{cases} \tag{10}$$

where c_s and c_p are the wave velocities of P waves and SV waves, respectively. The delay times Δt_1, Δt_2, Δt_3, and variables S_1 to S_6 are all boundary-dependent, which can be depicted as follows:

$$\begin{cases} \Delta t_1 = y\cos\alpha/c_s \\ \Delta t_2 = \left(2L_y - y\right)\cos\alpha/c_s \\ \Delta t_3 = \left(L_y - y\right)/\left(c_p\cos\beta\right) + \left(L_y - \left(L_y - y\right)\tan\alpha\tan\beta\right)\cos\alpha/c_s \end{cases} \quad (11)$$
$$S_1 = \frac{G\sin 2\alpha}{c_s},\ S_2 = -1,\ S_3 = \frac{\lambda+2G\sin^2\beta}{c_p},$$
$$S_4 = \frac{G\cos 2\alpha}{c_s},\ S_5 = 1,\ S_6 = -\frac{G\sin 2\beta}{c_p}$$

On the bottom boundary, they became:

$$\begin{cases} \Delta t_1 = x\sin\alpha/c_s \\ \Delta t_2 = \left(2L_y + x\tan\alpha\right)\cos\alpha/c_s \\ \Delta t_3 = L_y/\left(c_p\cos\beta\right) + \left(L_y\cos\alpha + x\sin\alpha - L_y\tan\beta\sin\alpha\right)/c_s \end{cases} \quad (12)$$
$$S_1 = \frac{G\cos 2\alpha}{c_s},\ S_2 = 1,\ S_3 = -\frac{G\sin 2\beta}{c_p},$$
$$S_4 = \frac{G\sin 2\alpha}{c_s},\ S_5 = 1,\ S_6 = \frac{\lambda+2G\cos^2\beta}{c_p}$$

On the right boundary, the stresses were the same but in opposite directions to those on the left boundary, and for the displacement, the delay times were Δt_1, Δt_2, and Δt_3, each of them increased by $L_x\sin\alpha/c_s$ for the additional travel distance.

3.2.2. P Waves

Figure 4 presents a plane study area that was subjected to oblique incident P waves. Similar to the oblique incident SV waves, each truncated boundary was subjected to three waves that involved one incident wave and two reflected waves, as shown in Figure 4. When node B, one of the joints on the left truncated boundary, were considered, the incident seismic waves of node B reached the boundary directly (incident P waves) or through reflection after first reaching the ground surface (reflected P waves and reflected SV waves). The displacement and velocity of the incident P waves are denoted as $u_p(t)$ and$\dot{u}_p(t)$, respectively.

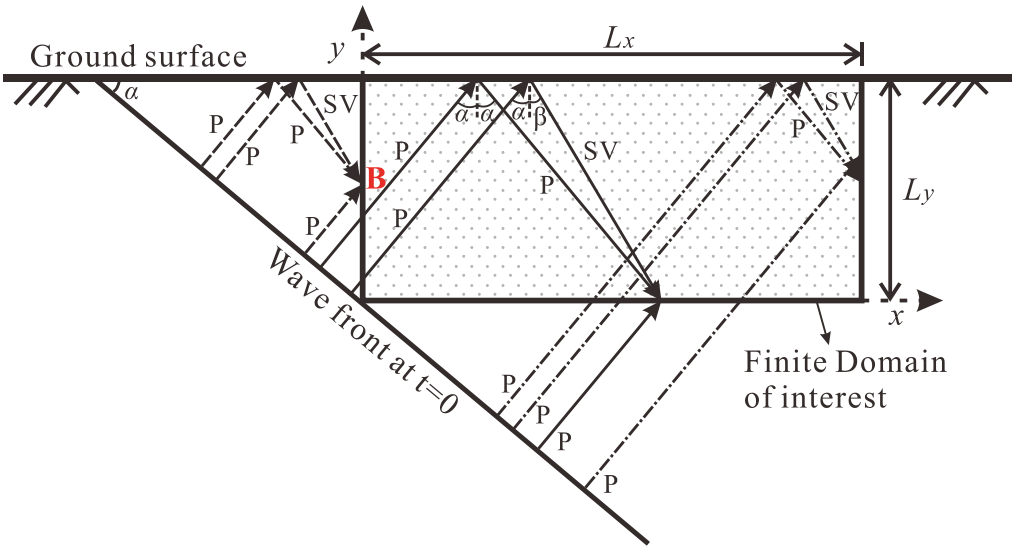

Figure 4. Sketch of the seismic waves on truncated boundary by obliquely incident P waves.

Consequently, the free-field motion and associated stress (in terms of their x and y components) can be induced at the given point B (x_1, y_1) as follows:

$$\begin{cases} u_{lx}(t) = u_p(t-\Delta t_4)\sin(\alpha) + A_3 u_p(t-\Delta t_5)\sin(\alpha) + A_4 u_s(t-\Delta t_6)\cos(\beta) \\ u_{ly}(t) = u_p(t-\Delta t_4)\cos(\alpha) - A_3 u_p(t-\Delta t_5)\cos(\alpha) + A_4 u_s(t-\Delta t_6)\sin(\beta) \\ \dot{u}_{lx}(t) = \dot{u}_p(t-\Delta t_4)\sin(\alpha) + A_3 \dot{u}_p(t-\Delta t_5)sin(\alpha) + A_4 \dot{u}_s(t-\Delta t_6)\cos(\beta) \\ \dot{u}_{ly}(t) = \dot{u}_p(t-\Delta t_4)\cos(\alpha) - A_3 \dot{u}_p(t-\Delta t_5)cos(\alpha) + A_4 \dot{u}_s(t-\Delta t_6)\sin(\beta) \end{cases} \tag{13}$$

$$\begin{cases} \sigma_{lx} = S_7\left(\dot{u}_p(t-\Delta t_4) + S_8 A_3 \dot{u}_p(t-\Delta t_5)\right) + S_9 A_4 \dot{u}_s(t-\Delta t_6) \\ \sigma_{ly} = S_{10}\left(\dot{u}_p(t-\Delta t_4) + S_{11} A_3 \dot{u}_p(t-\Delta t_5)\right) + S_{12} A_4 \dot{u}_s(t-\Delta t_6) \end{cases} \tag{14}$$

where A_3 and A_4 are the amplitude ratios (denoted as the reflected P waves and reflected SV waves to the incident P waves). Δt denotes the delay time of waves from the wavefront at t = 0 to the boundary node (node B). α and β are the angles between the vertical direction and reflected P waves together with the reflected SV waves, respectively. A_3, A_4 and β can be expressed as follows:

$$\begin{cases} A_3 = \frac{{c_s}^2 \sin 2\alpha \sin 2\beta - {c_p}^2 \cos^2 2\beta}{{c_s}^2 \sin 2\alpha \sin 2\beta + {c_p}^2 \cos^2 2\beta} \\ A_4 = \frac{2 c_p c_s \sin 2\alpha \cos 2\beta}{{c_s}^2 \sin 2\alpha \sin 2\beta + {c_p}^2 \cos^2 2\beta} \\ \beta = \arcsin\left(\frac{c_s \sin\alpha}{c_p}\right) \end{cases} \tag{15}$$

where c_s and c_p are the wave velocities of P waves and SV waves, respectively. The delay times Δt_4, Δt_5, Δt_6, and the variables S_7 to S_{12} are all boundary-dependent, which can be depicted as follows:

$$\begin{cases} \Delta t_4 = y\cos\alpha / c_p \\ \Delta t_5 = \left(2L_y - y\right)\cos\alpha / c_p \\ \Delta t_6 = \left(L_y - y\right)/\left(c_s\cos\beta\right) + \left(L_y - \left(L_y - y\right)\tan\alpha\tan\beta\right)\cos\alpha / c_p \end{cases} \tag{16}$$
$$S_7 = \frac{\lambda + 2G\sin^2\alpha}{c_p},\ S_8 = 1,\ S_9 = \frac{G\sin 2\beta}{c_s},$$
$$S_{10} = \frac{G\sin 2\alpha}{c_p},\ S_{11} = -1,\ S_{12} = -\frac{G\cos 2\beta}{c_s}$$

On the bottom boundary, they became:

$$\begin{cases} \Delta t_4 = x\sin\alpha / c_p \\ \Delta t_5 = \left(2L_y + x\tan\alpha\right)\cos\alpha / c_p \\ \Delta t_6 = L_y/\left(c_s\cos\beta\right) + \left(L_y\cos\alpha + x\sin\alpha - L_y\tan\beta\sin\alpha\right)/c_p \end{cases} \tag{17}$$
$$S_7 = \frac{G\sin 2\alpha}{c_p},\ S_8 = -1,\ S_9 = -\frac{G\cos 2\beta}{c_s},$$
$$S_{10} = \frac{\lambda + 2G\cos^2\alpha}{c_p},\ S_{11} = 1,\ S_{12} = -\frac{G\sin 2\beta}{c_s}$$

On the right boundary, the stresses were the same but in directions opposite to those on the left boundary, and for the displacement, the delay times were Δt_4, Δt_5, and Δt_6,, each of which increased by $L_x \sin\alpha / c_p$ for the additional travel distance.

3.3. Verification

The incident seismic waves were implemented using the ABAQUS software, together with a self-developed MATLAB program. The specific implementation is described in the flowchart illustrated in Figure 5. Two numerical test examples were used to verify the validity of the oblique incident seismic waves. One was the propagating process of oblique incident waves in a truncated region, which was considered to explore the accuracy of the input method in a semi-infinite field. The other was the response of a semicircular canyon input by oblique incident waves, which was aimed at determining the accuracy of the simulation in the topography.

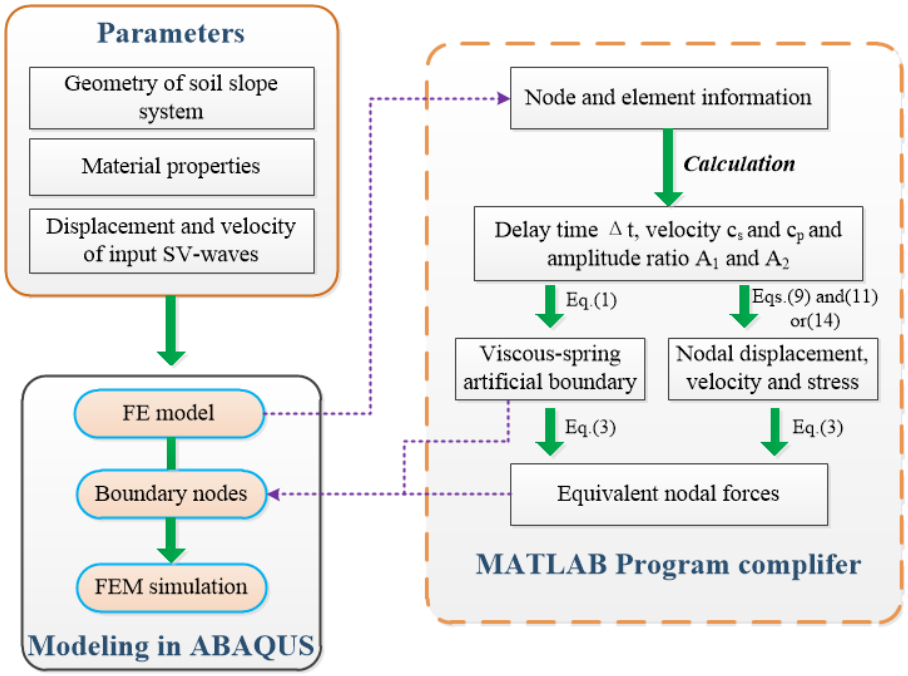

Figure 5. Flow chart for input seismic waves implemented in ABAQUS.

3.3.1. Test Example 1

A truncated rectangular domain was adopted to simulate the propagation process of oblique incident waves in a semi-infinite field, as depicted in Figure 6a. The sizes of the truncated regions were as follows: L_x = 800 m and L_y = 400 m. The region was sufficiently large to detect the propagation of all the incident and reflected waves. The incident angles of the P waves and SV waves were assumed to be 30° and 18°, respectively.

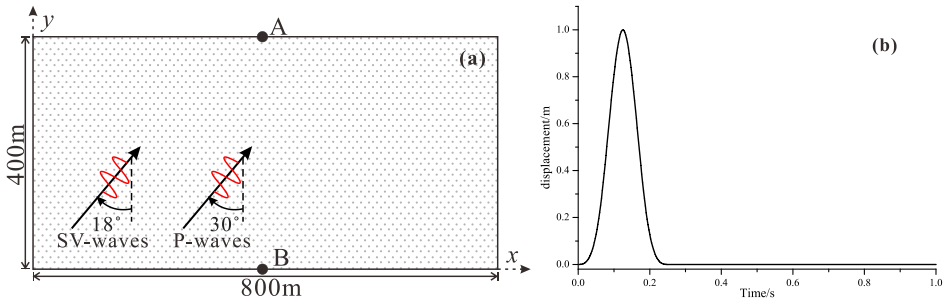

Figure 6. Numerical model and incident waves of test example 1: (**a**) finite element model and (**b**) displacement time history of incident waves.

The material parameters of the domain were as follows: Poisson's ratio = 0.25, elastic modulus = 1.25 Gpa and mass density, ρ = 2000 kg/m^3. Points A (400, 400) and B (400, 0) are the observation points. An impulse was adopted as an incident seismic wave, as shown in Figure 6b. The impulse equation is defined as follows [57]:

$$P(t) = 16P_0\left[G(t) - 4G\left(t - \frac{1}{4}\right) + 6G\left(t - \frac{1}{2}\right) - 4G\left(t - \frac{3}{4}\right) + G(t-1)\right] \quad (18)$$

where $G = (t/T_0)^3 H(t/T_0)$ $H(t)$ is the Heaviside function, P_0 is the peak value of an impulse, P_0 is set to 1.0 m; and T_0 is the acting time of the impulse, where T_0 = 0.25 s.

Figure 7 shows the displacement contours with the time of incident SV waves. As illustrated in the figures, the propagation processes of the incident waves and reflected waves at the ground surface were simulated effectively in a semi-infinite field. In addition,

the displacement time histories of the observation points (points A and B) are shown in Figure 8. As shown in the figures, the numerical results proposed by the input method were in good agreement with the analytical solutions, where the analytical solutions were calculated using the elastic wave propagation theory [58,59].

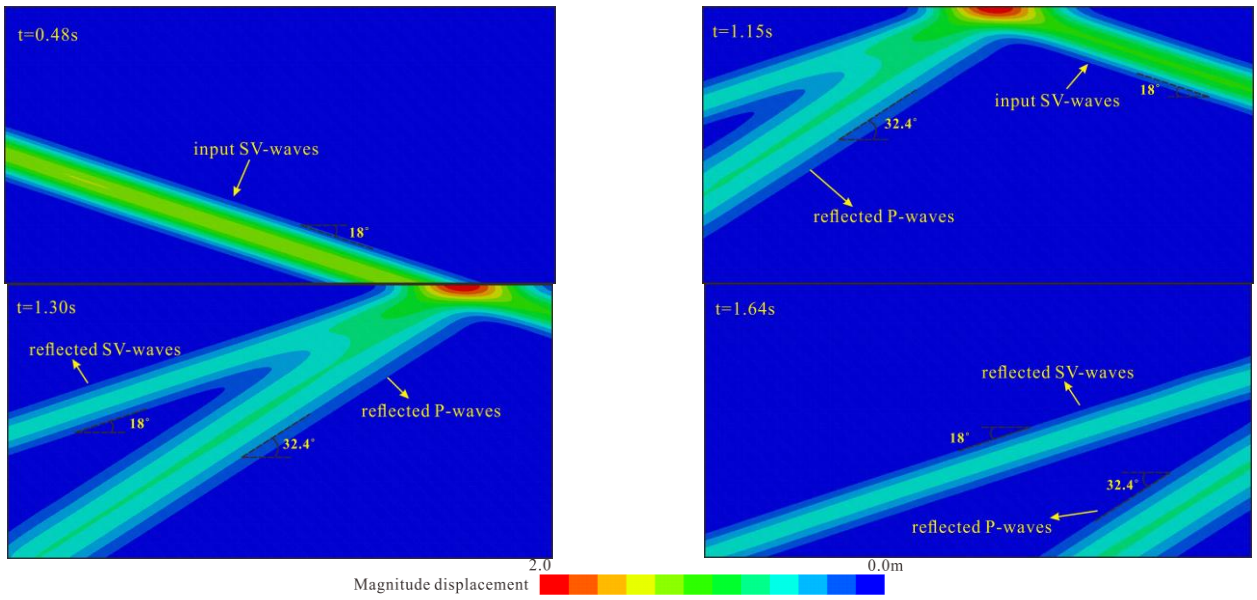

Figure 7. Displacement contours of SV waves propagated in semi-infinite space.

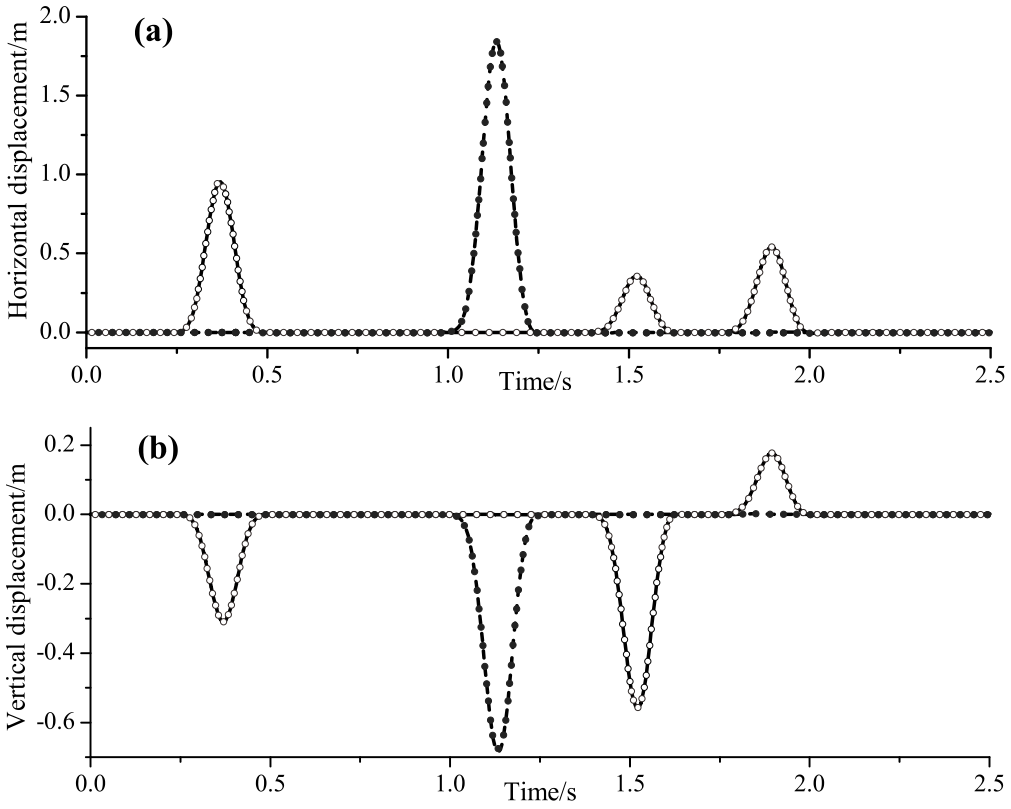

Figure 8. Displacement time history at observation points of incident SV waves: (**a**) horizontal displacement, and (**b**) vertical displacement (solid lines and dashed lines are numerical results of points A and B, respectively, with circles showing analytical solutions).

The displacement contours with the time of P waves in Figure 9 show the propagation processes of the incident waves and reflected waves at the ground surface. Meanwhile, the displacement contours and the displacement time histories of the observation points (points A and B) in Figure 10 both confirm that the input method was effective and precise in the semi-infinite field. Therefore, the oblique incident SV waves and P waves in a semi-infinite field could be simulated using the proposed input method, and the ability of the viscous-spring artificial boundary to absorb the scattered waves was also verified.

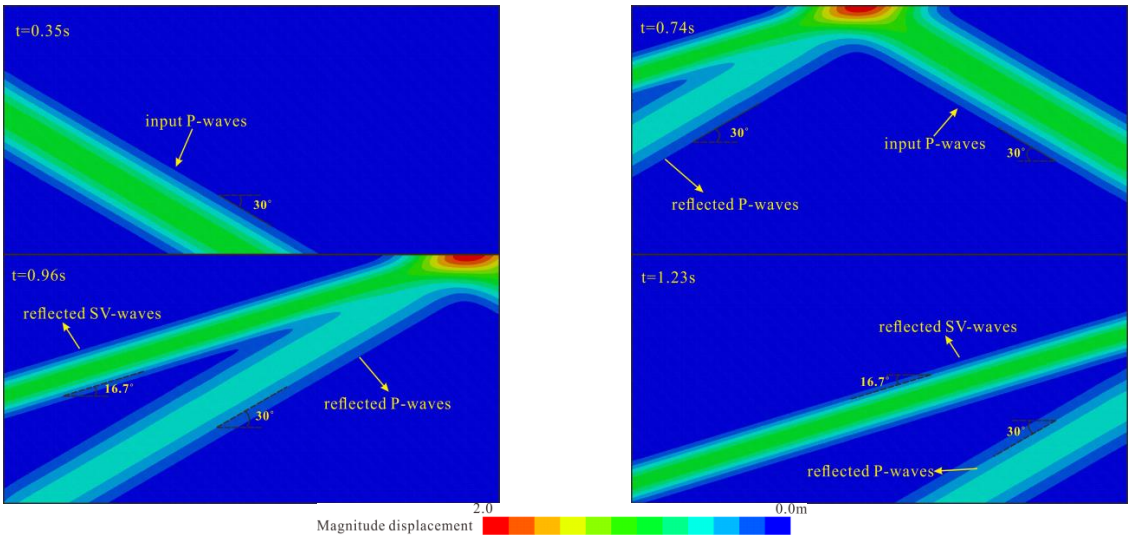

Figure 9. Displacement contours of P waves propagated in semi-infinite space.

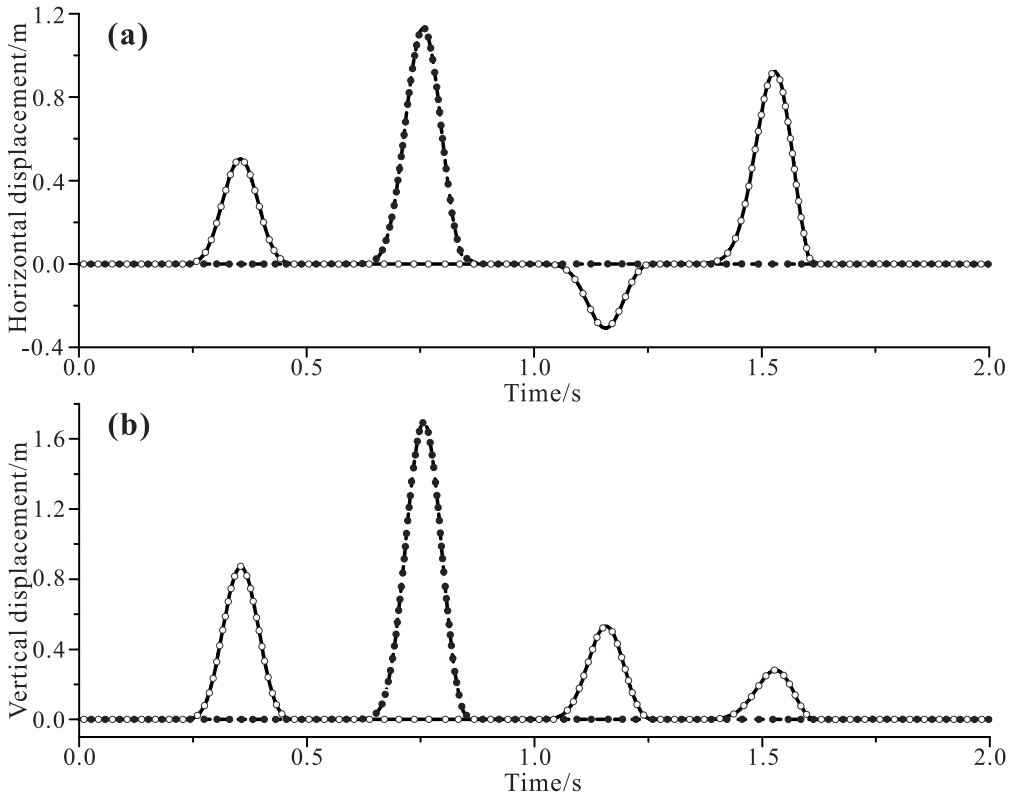

Figure 10. Displacement time history at observation points of incident P waves: (**a**) horizontal displacement, and (**b**) vertical displacement (solid lines and dashed lines are numerical results of points A and B, respectively, with circles showing analytical solutions).

3.3.2. Test Example 2

A truncated rectangular domain with a semicircular canyon is shown in Figure 11a. The truncated region was $0 \leq x \leq 200$ m, $0 \leq y \leq 200$ m and the radius of the canyon was 25 m. The material parameters of the ground were as follows: Poisson's ratio = 0.3, elastic modulus = 208 MPa and mass density, $\rho = 2000$ kg/m^3. A Ricker wavelet was adopted as the incident wave. The acceleration-time history of the wave is illustrated in Figure 11b. The time history of the Ricker wavelet was defined as follows:

$$R(t) = \left(1 - 2\pi^2 f_0^2 t^2\right) \exp\left(-\pi^2 f_0^2 t^2\right) \tag{19}$$

with an excitation frequency f_0 of 4.0 Hz.

The incident angles had values of 25° under SV waves and 30° under P waves. Figures 12 and 13 show the horizontal displacement amplification ratios U_h and vertical displacement amplification ratios U_v of the ground surface on the canyon with incident SV waves and incident P waves, respectively. U_h is defined as the ratio of the horizontal displacement on the ground surface to the input horizontal displacement, and U_v is the ratio of the vertical displacement. The numerical results presented in Figures 12 and 13 were in good agreement with the analytical solutions proposed by Wong [60]. Therefore, in the topographic analysis, the proposed input method could effectively simulate the propagation process of oblique incident seismic waves, and the viscous-spring artificial boundary could absorb the scattered waves perfectly because of the topography.

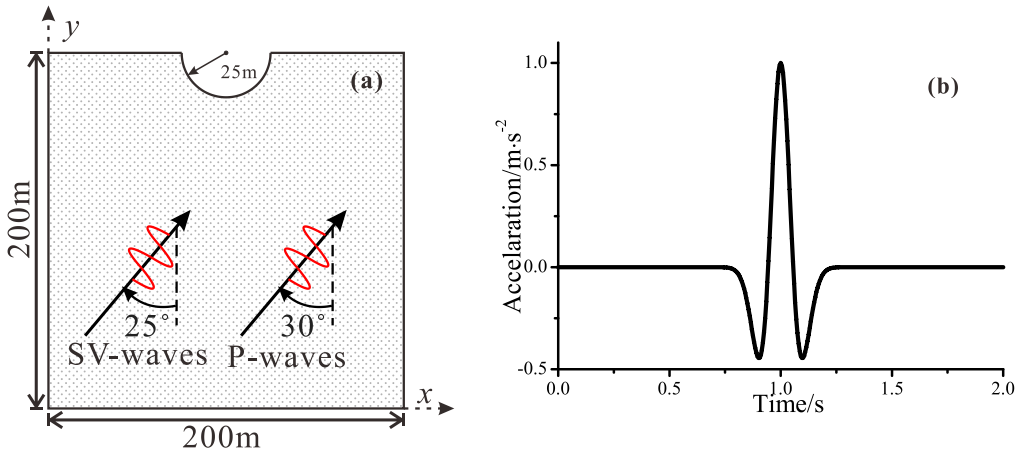

Figure 11. Numerical model and input waves of test example 2: (**a**) finite element model and (**b**) acceleration time-history of incident waves.

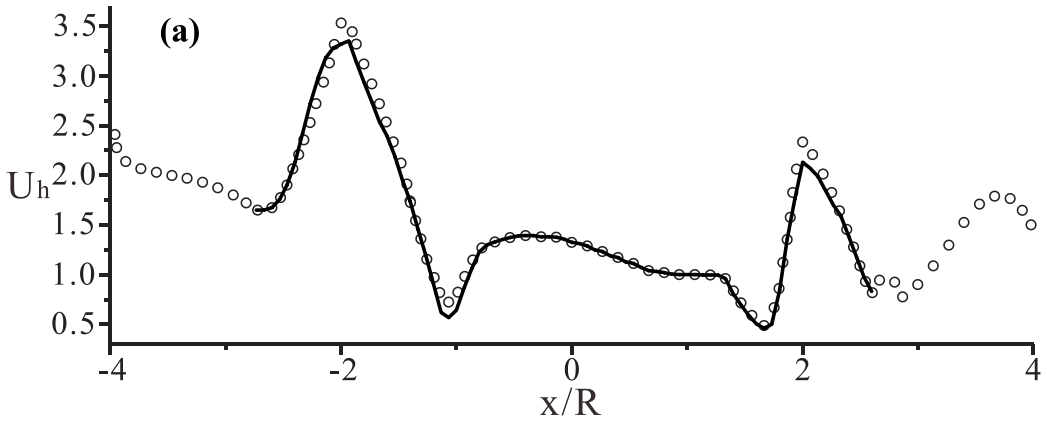

Figure 12. *Cont.*

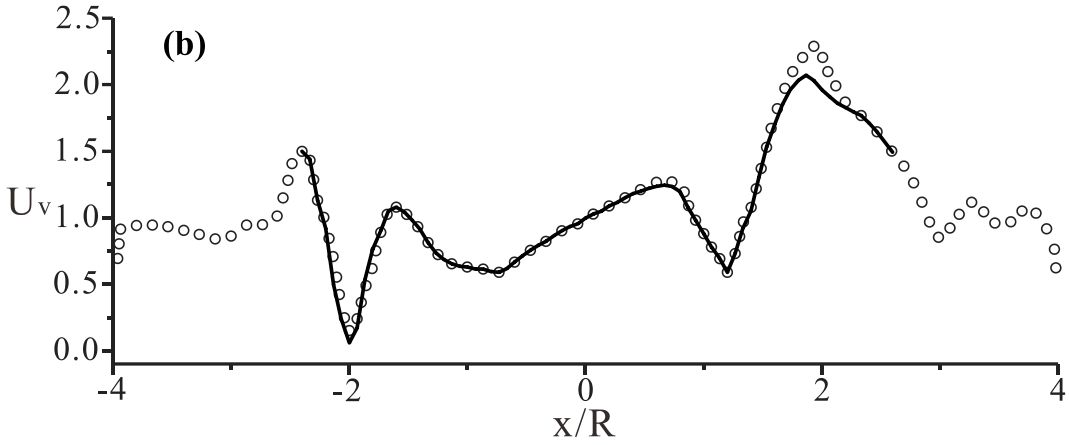

Figure 12. Displacement amplification ratios of ground under incident SV-waves with angle of 25°: (**a**) horizontal ratios and (**b**) vertical ratios (solid lines are analytical solutions by Wong [60] and circles are numerical results of finite element method based on ABAQUS).

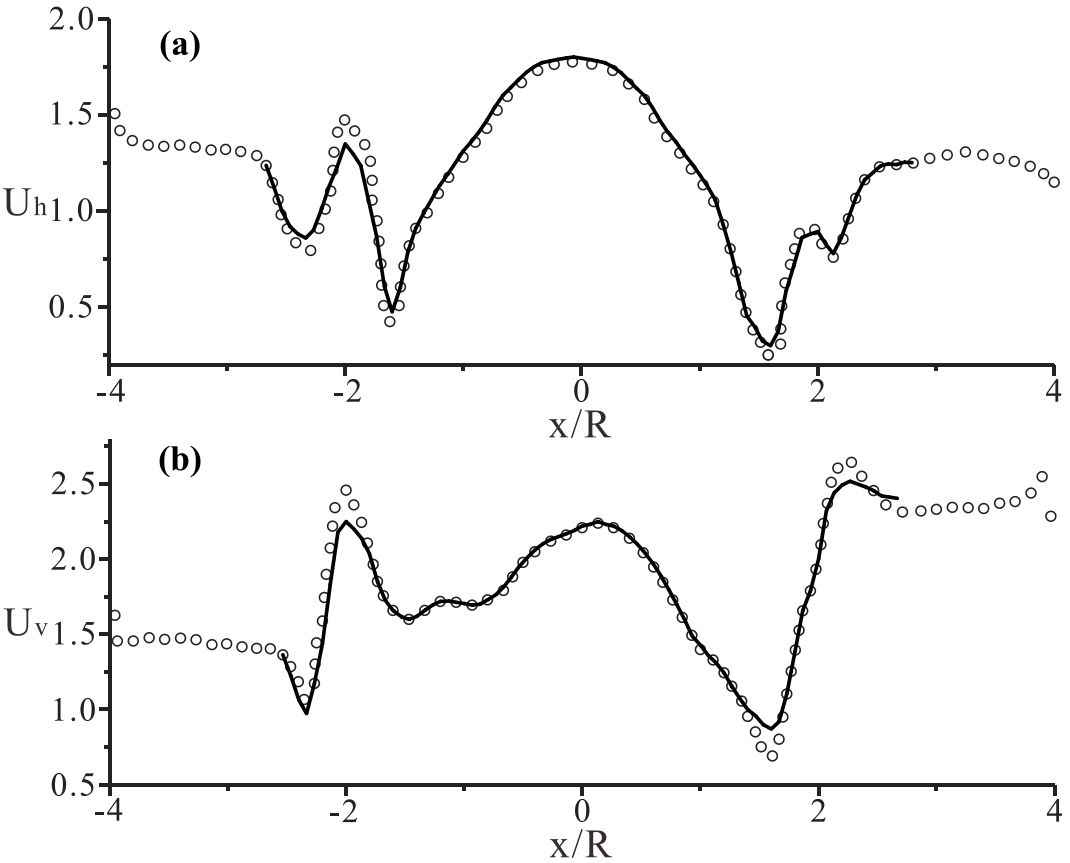

Figure 13. Displacement amplification ratios of ground under incident P-waves with angle of 30°: (**a**) horizontal ratios and (**b**) vertical ratios (solid lines are analytical solutions by Wong [60] and circles are numerical results of finite element method based on ABAQUS).

4. Discussion and Results

A schematic of the numerical model is illustrated in Figure 1. The mesh type of this numerical model is quadrilateral element. A Ricker wavelet with a predominant frequency of 4.0 Hz was employed as the incident wave to investigate the wave patterns, materials and slope geometries based on the seismic responses. The acceleration-time history of the incident wave, which was input from the left bottom of the model, is illustrated in Figure 10b. To analyze the topographic effects, the acceleration amplification ratio was applied, which is the ratio of the peak acceleration of the reflected waves at each point on the surface to that of the incident seismic waves [36,45]. The horizontal and vertical acceleration amplification ratios r_{h} and r_{v} are defined in Equations (20) and (21), respectively. For a given wave, r_{h} and r_{v} are the values of the acceleration amplification ratio r for the horizontal and vertical components, respectively. $r = \sqrt{{r_{\mathrm{h}}}^2 + {r_v}^2}$ defines zones of the net amplification of ground acceleration with respect to the energy carried by the incoming waves.

$$r_{\mathrm{h}} = \frac{\max(|a_{\mathrm{h}}|)}{\left|a_{\mathrm{h,input}}\right|} \tag{20}$$

$$r_{\mathrm{v}} = \frac{\max(|a_{\mathrm{v}}|)}{\left|a_{\mathrm{v,input}}\right|} \tag{21}$$

where $\max(|a_{\mathrm{h}}|)$ and $\max(|a_{\mathrm{v}}|)$ are the peak horizontal (h) and peak vertical (v) acceleration at the observation points along the slope ridges and slope crests, respectively; and $\left|a_{\mathrm{h,input}}\right|$ and $\left|a_{\mathrm{v,input}}\right|$ are the horizontal (h) and vertical (v) acceleration, respectively.

In this study, the wave patterns were discussed based on the P waves and the SV waves owing to the specific focus on the effects of body waves. In addition, the impact of the materials was investigated in terms of the relative hardness and softness between the slopes and foundations. The shear waves of different materials on the slope topographies are presented in Table 1. Furthermore, the geometries of slopes with varying slope heights, widths and inclinations are discussed. The slope height H is a normalized height that is related to the wavelength λ [29,36], and it varies among 0.2λ, 0.5λ, 1.0λ and 2.0λ. The width of the slope crest W varied from 50 to 400 m, and the intermediate values were 100 m and 200 m. The slope inclination i varied between 26.6°, 33.7°, 45°, 55° and 63.4°, corresponding to width-depth ratios (defined as cot$i$) of 2.0, 1.5, 1.0, 0.7 and 0.5. All the influencing factors (wave patterns, materials and geometries) were based on the varied directions of incident waves, which were input from the left bottom of the topography with incident angles θ in the range of 0° to 30°, sampled at 5° intervals.

4.1. Effects of Wave Patterns

Wave patterns, that is, P waves and SV waves, were discussed based on three different slope topographies with varied angles of incident waves. Three models with different slope widths, W = 0 m, 100 m and 400 m, were built to evaluate the effect of wave patterns on ground motion amplification. The original model had a height of 100 m and an inclination of 1.0 (45°); meanwhile, the materials of the slope were regarded as homogeneous. The acceleration amplification ratios of the P waves and SV waves at different seismic wave inclinations are summarized in Figure 14.

The acceleration amplification ratios of SV waves were larger than those of P waves at a specific slope topography. The slope width became wider and the amplification ratios gradually decreased for each slope pattern. With an increase in the angle of incidence, the acceleration amplification effects moved away from the epicenter and the maximum acceleration amplification ratios were obtained when the incident angles fluctuated between 20° and 30°, which were especially clear under SV waves. Thus, the pattern of amplification of the SV waves was verified to be stronger in the slope topography, and the evolution was the same as that of the findings of Meunier [35] (depicted as the slope configurations of Figure 14a).

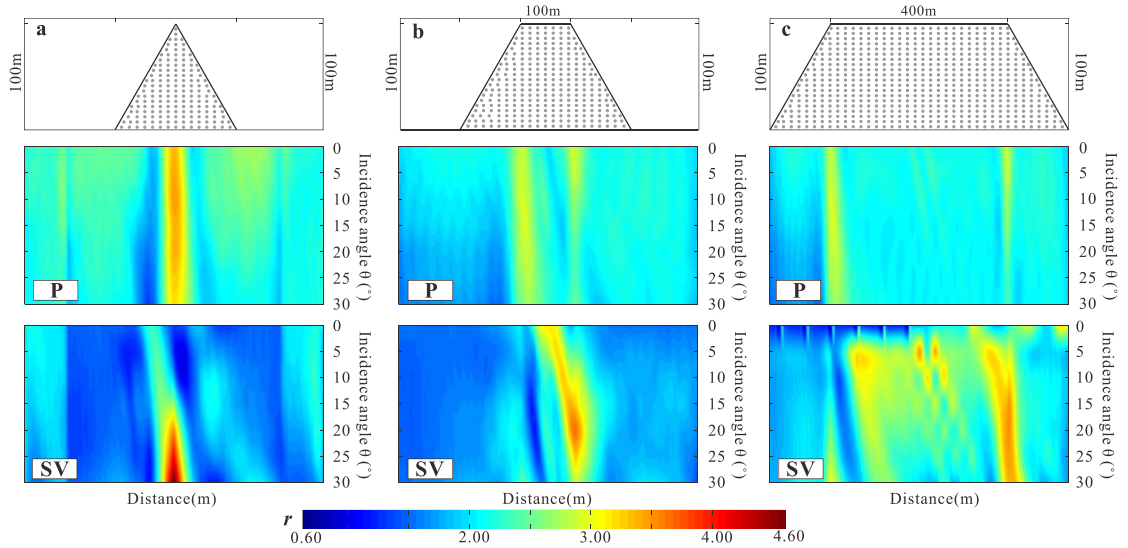

Figure 14. Variations of the seismic responses along the slope ridges of the real amplification ratio (*r*) of PGA with varied angles of wave incidence at P waves and SV waves. (**a**) slope width of 0 m, (**b**) slope width of 100 m, (**c**) slope width of 400 m.

4.2. Effects of Materials

In this section, materials are discussed based on the specific slope topography with varying directions of incident waves. Three models, wherein the slope is soft whereas the foundation is hard, the slope and foundation are both the same, and the slope is hard whereas the foundation is soft, were built to investigate the effects of the materials on the ground motion amplification of slope topography. The investigated model was 100 m high, 100 m wide and 1.0 (45°) in inclination. The so-called softness and hardness of the materials in the slopes or foundations in Figure 15 is in contrast to that of the materials in the foundation (the foundation materials are fixed); that is, the materials of the slope changed from soft to hard (from left to right in Figure 15). The acceleration amplification ratios of the different materials at different incident angles are summarized in Figure 15.

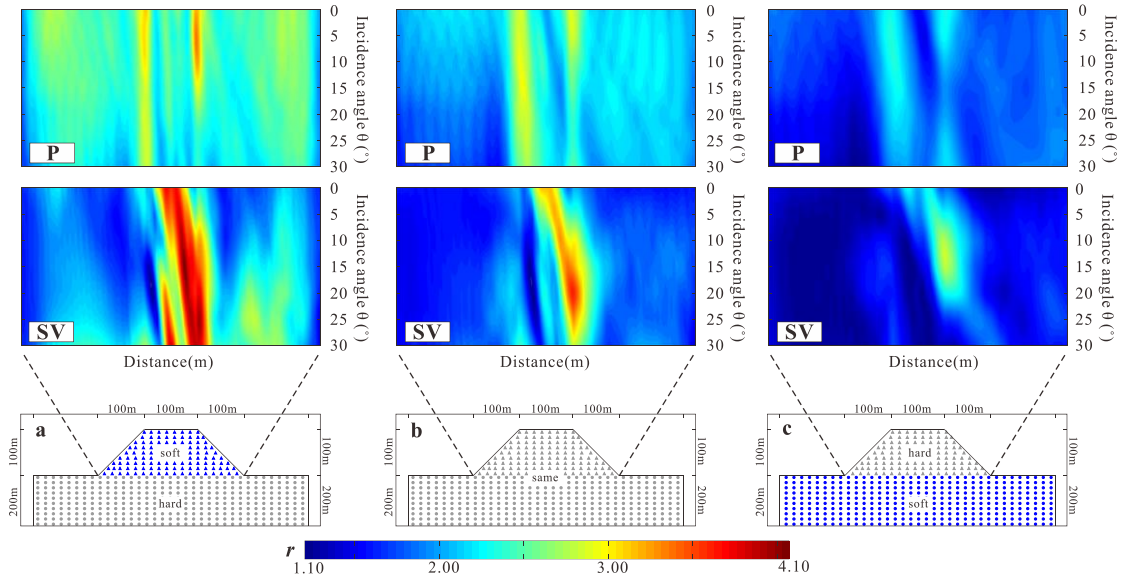

Figure 15. Variations of the seismic responses along the slope ridges and the slope crests of the real amplification ratio (*r*) of PGA with varied angles of wave incidence under different materials. (**a**) slope soft while foundation hard, (**b**) slope and foundation are same, (**c**) slope hard while foundation soft.

In Figure 15, the acceleration amplification ratios of the SV waves were larger than those of the P waves for each material. The ratios gradually decreased as the materials in the slope varied from soft to hard; that is, the soft materials intensified the amplification whereas the hard materials alleviated the amplification in the slope topography. In addition, the maximum acceleration amplification ratios were acquired when the incident angles fluctuated between 10° and 25° under SV waves incidence and fell between 0° and 10° under P waves incidence. Consequently, the slope topographies that covered soft materials were more harmful during earthquake events, and the maximum ground motions of slope topographies were usually in a certain direction of oblique incident seismic waves.

The synthetic accelerograms of the horizontal and vertical components of SV waves and P waves with incident angles of 0° and 30°are presented in Figures 16 and 17, respectively. In the figures, "soft-hard" was the abbreviation of "the slope is soft and the foundation is hard," which corresponded to the situation of "a" in Figure 15; "same" referred to the situation of "b" in Figure 15, and "hard-soft" was marked as the situation of "c" in Figure 15.

As illustrated in the figures, the soft materials led to intense amplification of the ground motions, whereas the hard materials caused de-amplification. The scattered waves under the soft materials were abundant, whereas they were weakened in the hard materials. These evolutions were observed in the horizontal components of the SV waves and the vertical components of the P waves. In addition, compared with the scattered waves at 0° incidence and 30° incidence in Figures 16 and 17, the scattered waves were much more abundant at the oblique incident waves owing to the added refraction effects by the oblique directions of incident waves. In summary, the intense ground motions with soft materials in slope topography could be explained by the abundantly scattered waves, and this phenomenon would aggravate at oblique incident waves.

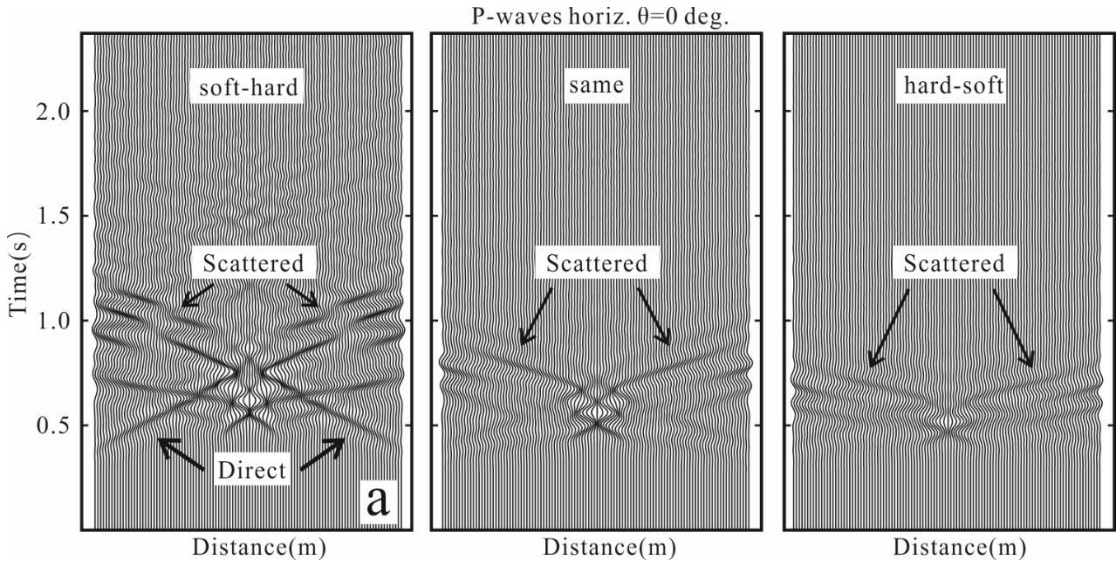

Figure 16. *Cont.*

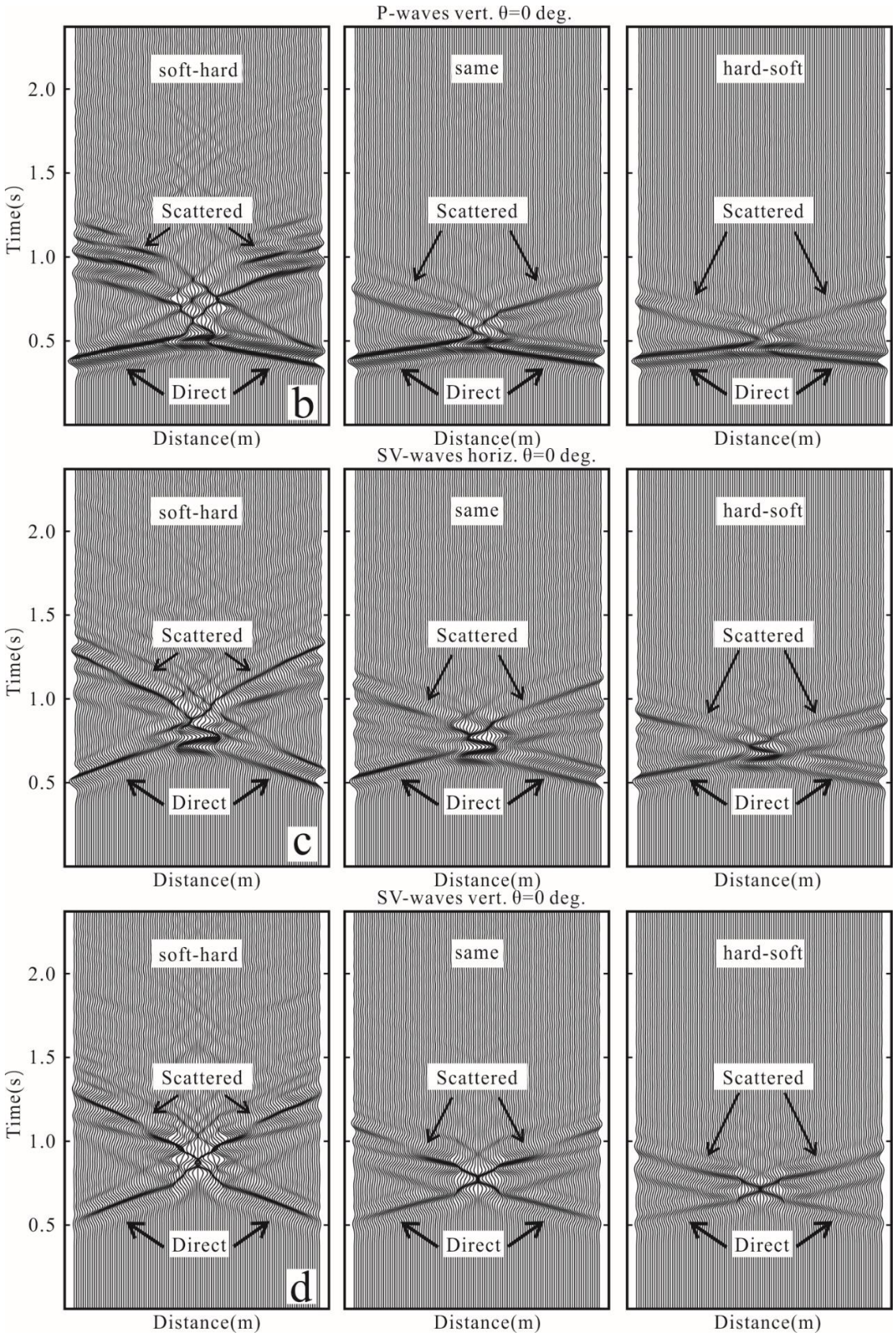

Figure 16. Synthetic accelerogram (accelerations recorded along the ground with time) generated along the topographic profile, plotted from the horizontal or vertical components of P waves and SV waves arriving from the left of the model at an incident angle of 0, (**a**) horizontal P waves with vertical direction, (**b**) vertical P waves with vertical direction, (**c**) horizontal SV waves with vertical direction (**d**) vertical SV waves with vertical direction.

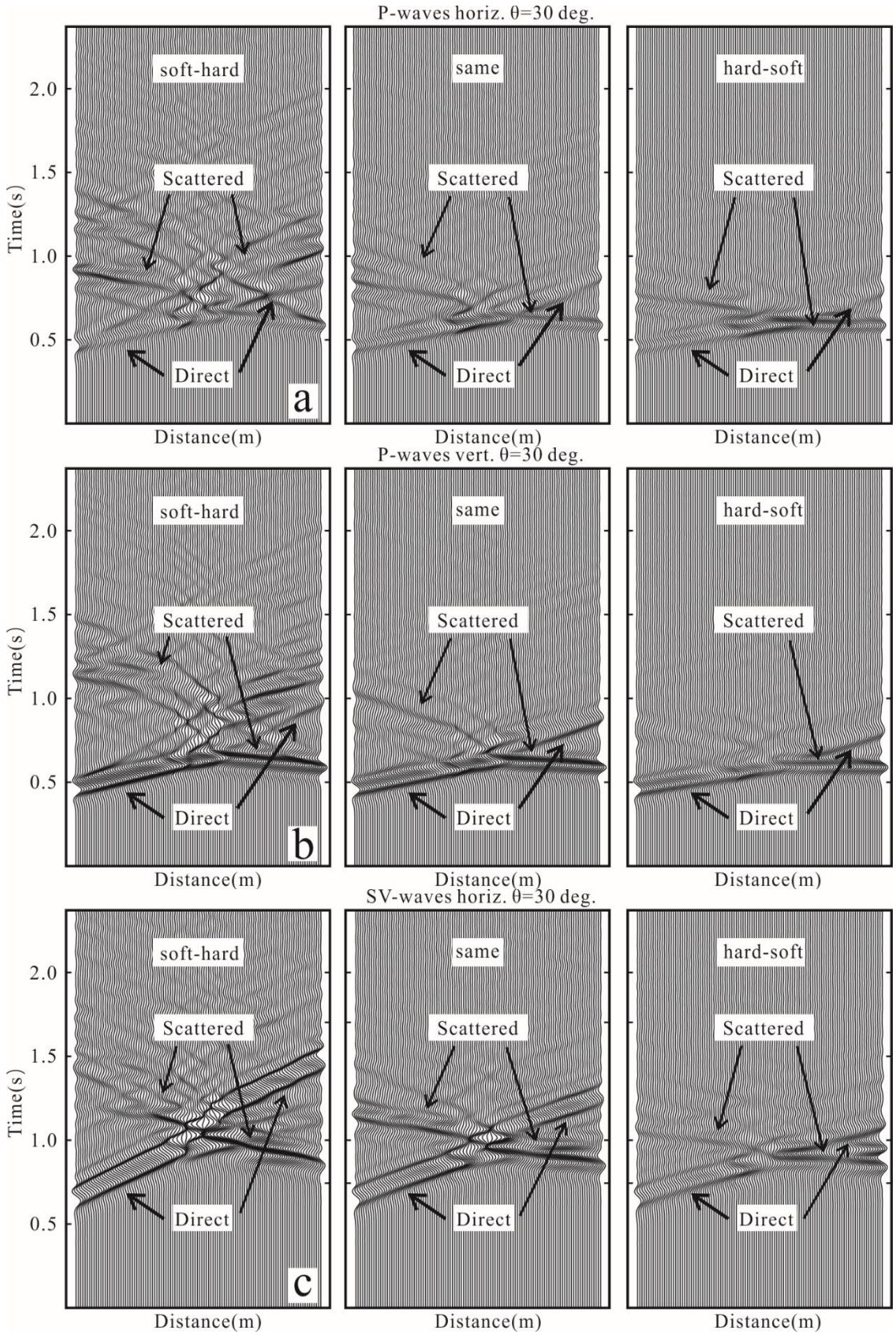

Figure 17. *Cont*.

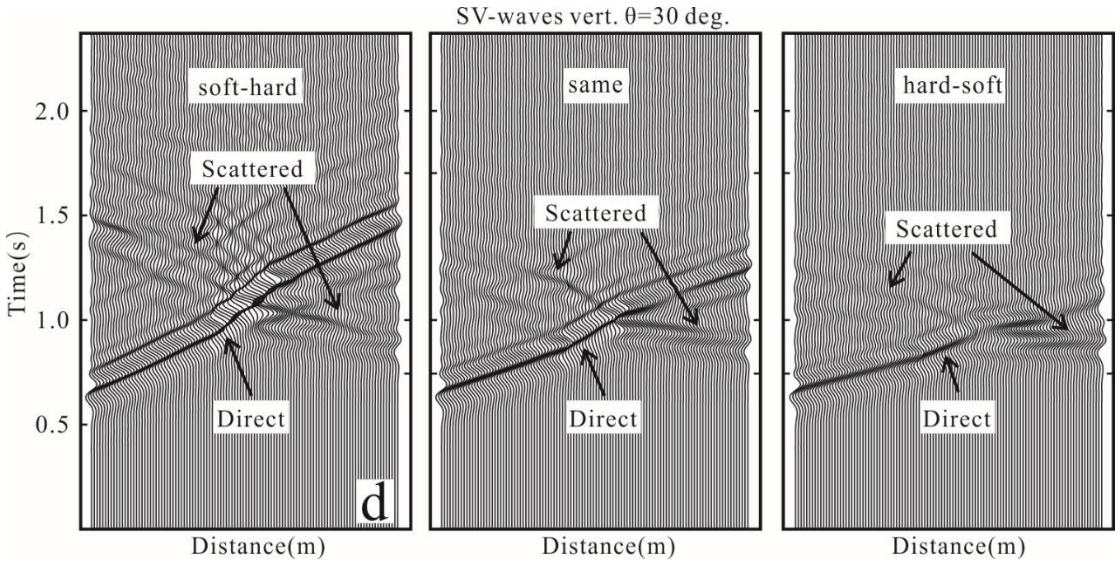

Figure 17. Synthetic accelerogram (accelerations recorded along the ground with time) generated along the topographic profile, plotted from the horizontal or vertical components of P waves and SV waves arriving from the left of the model at incident angle of 30°. (**a**) horizontal P waves with 30° directions, (**b**) vertical P waves with 30° directions, (**c**) horizontal SV waves with 30° directions (**d**) vertical SV waves with 30° directions.

4.3. Effects of Slope Geometries

According to the analysis of the impacts of wave patterns, the pattern of P waves was weak because of the amplification ratios of the ground motions, whereas that of SV waves was strong. Thus, the effects of the slope geometries were discussed only based on the SV waves rather than the P waves. In addition, the slope geometry changed the wave paths at various directions of wave incidence; thus, the materials of the slope topographies were assumed to be homogenous to eliminate the impacts of non-geometric factors. Consequently, this section, discusses the investigation of the effects of the slope geometries using homogeneous materials under SV incident waves.

4.3.1. Influence of Slope Height H

In this subsection, the slope height varied from 20 m, 50 m, 100 m, to 200 m, whereas the other geometrical parameters (slope widths and slope inclinations) remained the same. The acceleration amplification ratios along the slope surface are illustrated in Figure 18 with varying angles of incident waves.

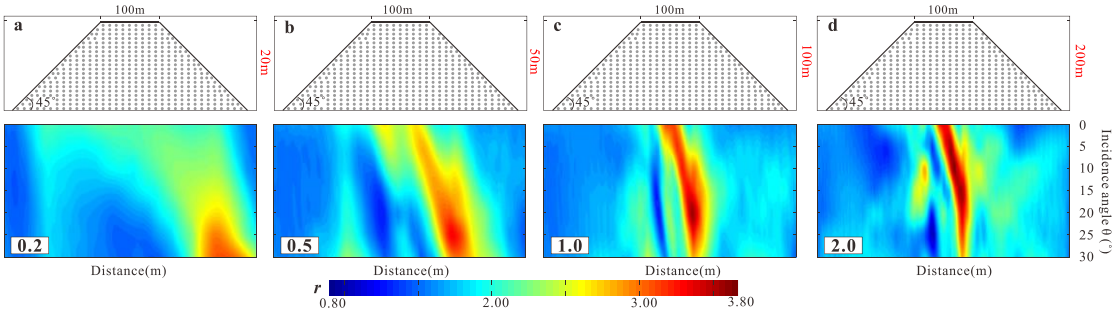

Figure 18. Variations of the seismic responses along the slope ridges and the slope crests of the real amplification ratio (*r*) of PGA with varied angles of wave incidence at different slope heights. (**a**) slope height of 20 m, (**b**) slope height of 50 m, (**c**) slope height of 100 m, (**d**) slope height of 200 m.

In Figure 18, different distributions of ground motions are presented with varying slope heights under SV incident waves. The acceleration amplification ratios rose signifi-

cantly with an increase in the slope height from 0.2λ to 2.0λ. The area of the maximum acceleration amplification ratios at each height moved to the center of the slope topography with an increase in slope height. In addition, the maximum acceleration amplification ratios could be obtained when the incident angles fell between 25° and 30° under a slope height of 0.2λ, whereas the maximum acceleration amplification ratios could be obtained when the incident angles fluctuated between 5° and 10° under a slope height of 2.0λ. Thus, the higher the slope heights, the closer the maximum acceleration amplification ratios were to the smaller inclinations of wave incidence. In summary, different slope heights influenced the wave aggregation at the crest; the higher the model, the larger the acceleration amplification ratios. The maximum ground motions were obtained in the oblique direction of the incident waves.

Moreover, the observation points (slope toe and slope crest) are presented with horizontal and vertical components in Figures 19 and 20, respectively, to analyze the comprehensive relations between the incident directions and slope heights.

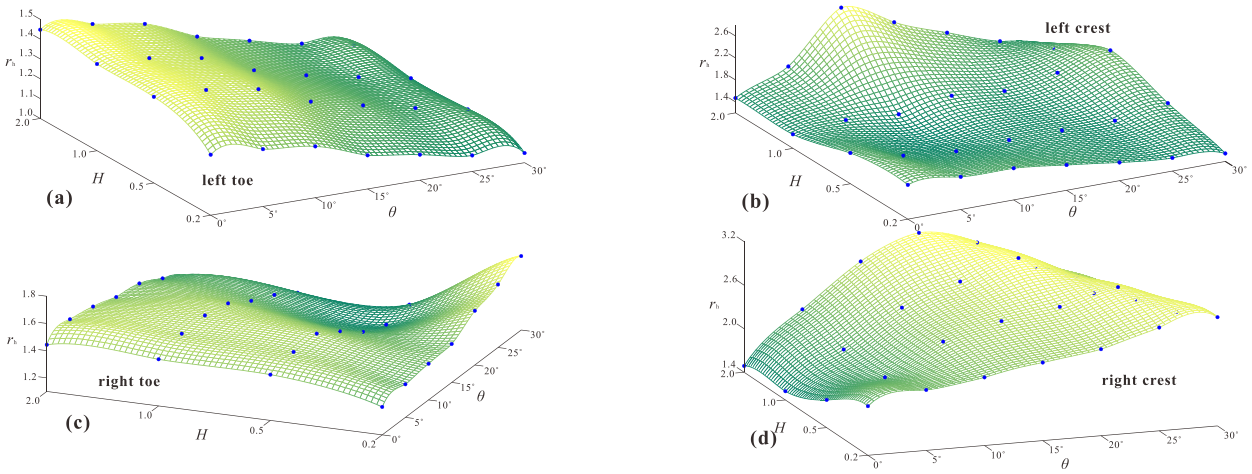

Figure 19. Variations of the horizontal amplification ratios (r_h) of PGA at the observation points ((**a**) left toe, (**b**) left crest, (**c**) right toe and (**d**) right crest) with varied angles of wave incidence at different slope heights.

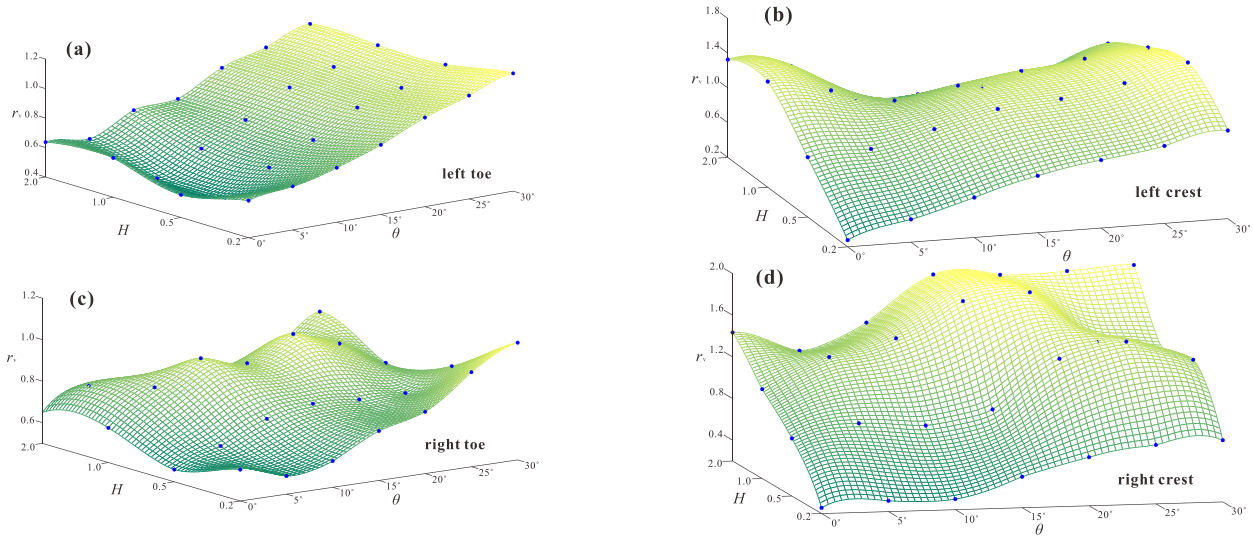

Figure 20. Variations of the vertical amplification ratios (r_v) of PGA at the observation points ((**a**) left toe, (**b**) left crest, (**c**) right toe and (**d**) right crest) with varied angles of wave incidence at different slope heights.

As shown in Figures 19 and 20, the variations in the amplification ratios at the slope toe were gentle. The horizontal amplification ratios at the left toe decreased with an

increase in the angle of incidence and increased with an increase in slope height. However, the vertical amplification ratios at the left toe increased with an increase in the angle of incidence, whereas their variations remained almost unchanged with varying slope heights. The horizontal amplification ratios at the right toe increased with an increase in the angle of wave incidence (at a slope height of 0.2), whereas they first increased and then decreased as the incident angle increased (at slope heights of 0.5, 1.0 and 2.0). The vertical amplification ratios of the right toe grew with an increase in the angle of incidence. Nevertheless, these ratios increased significantly at angles of 10° and 20° (at a slope height of 1.0). The variations above were in good agreement with the seismic responses of the ground motions in Figure 18 (at a slope height of 1.0), which indicated that the variations in the horizontal and vertical amplification ratios were non-monotonous at the slope toe.

The variations in the horizontal and vertical amplification ratios at the slope crest are complicated. The horizontal amplification ratios at the left crest monotonously rose or decreased with an increase in the angle of incidence (at slope heights of 0.2, 0.5 and 1.0). However, the horizontal ratios first increased and then decreased with an increase in the angles of incidence (at a slope height of 2.0). The maximum horizontal amplification ratios fell between 5° and 15° (at a slope height of 2.0). The horizontal amplification ratios at the right crest first increased and then decreased as the incident angle increased, and the maximum horizontal amplification ratios moved from the an incident angle of 30° to those at 15° as the slope height increased. The vertical amplification ratios of the left crest increased with an increase in the angle of incidence, and the maximum vertical amplification ratios of the left crest were obtained at a slope height of 1.0. The vertical amplification ratios of the right crest increased with an increase in the angle of incidence (at slope heights of 0.2 and 0.5). The variations in the vertical amplification ratios of the right crest were intensely complicated (at slope heights of 1.0 and 2.0), and the maximum ratios were obtained when the incident angles fell between 10° and 20°.

In summary, the variations in the amplification ratios at the slope toe were monotonous, that is, the ground motions changed regularly with varying incident angles and heights. Nonetheless, the variations in ground motions at the slope crest were complicated owing to the interactions between the input waves and the reflected waves in the topography.

4.3.2. Influence of the Width of Slope Crest W

The width of the slope crest varied from 50 m, 100 m and 200 m to 400 m, whereas the other geometrical parameters (slope heights and slope inclinations) remained the same. The acceleration amplification ratios along the slope surface are illustrated in Figure 21 with varying incident angles.

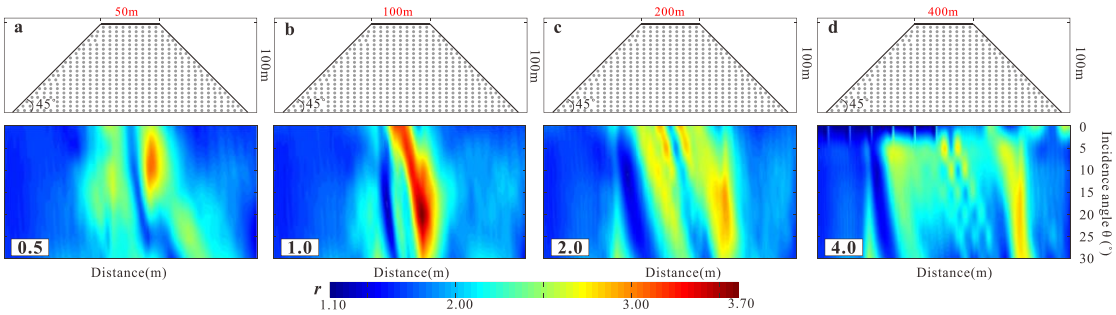

Figure 21. Variations of the seismic responses along the slope ridges and slope crests of the real amplification ratios (*r*) of PGA with varied angles of wave incidence at different slope widths, (**a**) slope width of 50 m, (**b**) slope width of 100 m, (**c**) slope width of 200 m (**d**) slope width of 400 m.

As illustrated in Figure 21, the acceleration amplification ratios at a slope width of 1.0 H were the greatest. This phenomenon can be indicated by the resonance of the model sizes and wavelengths. The ground motions were concentrated on the slope crest, especially

when the slope width was 4.0 H. In addition, the maximum acceleration amplification ratios were obtained when the incident angles were between 5° and 10° at a width of 0.5 H, whereas the ratios reached a maximum when the incident angles fluctuated between 25° and 30° at a slope width of 4.0 H. Thus, the wider the slope crests, the closer the maximum acceleration amplification ratios were to the greater inclinations of incident waves. In summary, the energies of earthquake waves were mainly concentrated at the crest of the slope topography. The maximum ground motions occurred as the width of the slope model was nearly one wavelength, especially in certain directions of seismic incident waves.

Moreover, the observation points (slope toe and slope crest) are analyzed in Figures 22 and 23, respectively. All the observation points are illustrated based on the horizontal and vertical amplification ratios, to analyze the comprehensive relations between the incident angles and slope widths.

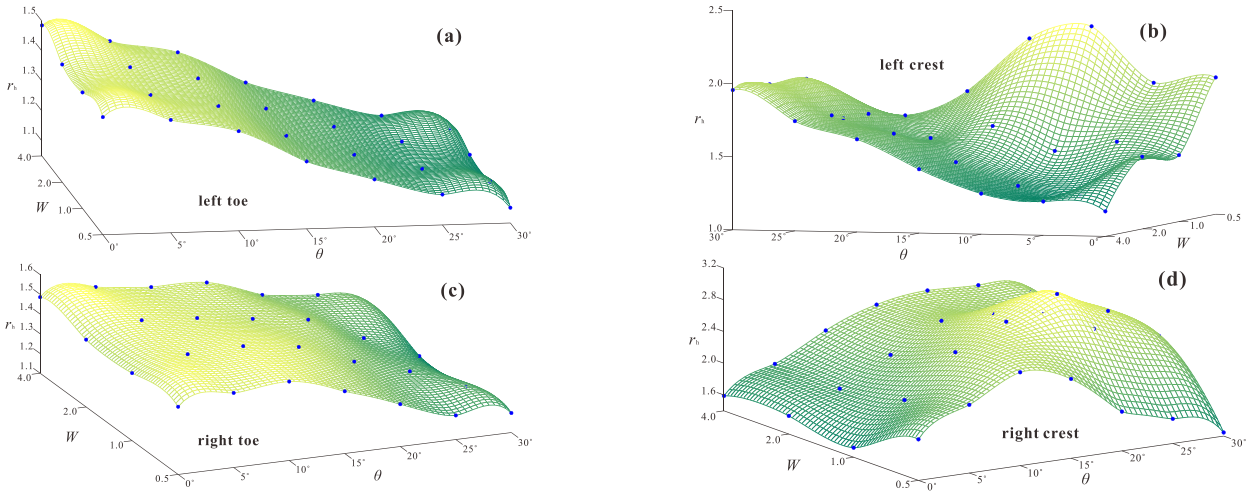

Figure 22. Variations of the horizontal amplification ratios (r_h) of PGA at the observation points ((**a**) left toe, (**b**) left crest, (**c**) right toe and (**d**) right crest) with varied angles of wave incidence at different slope widths.

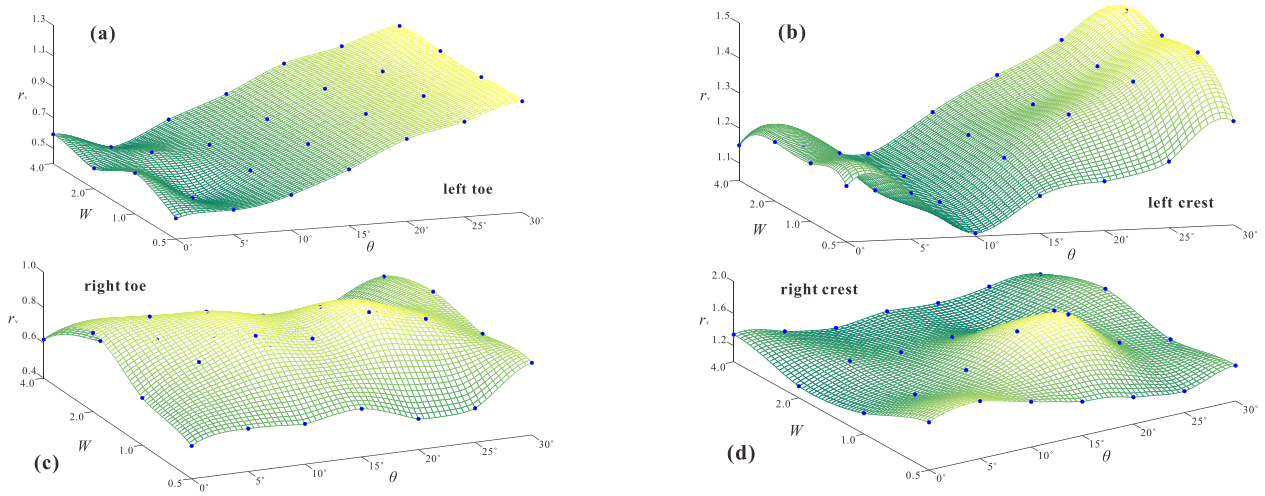

Figure 23. Variations of the vertical amplification ratios (r_v) of PGA at the observation points ((**a**) left toe, (**b**) left crest, (**c**) right toe and (**d**) right crest) with varied angles of wave incidence at different slope widths.

The horizontal amplification ratios at the slope toe decreased monotonously with an increase in the incident angle, whereas they increased as the slope width increased. The vertical amplification ratios at the left toe increased with an increase in the incident angle.

The vertical amplification ratios at the right toe reached a maximum when the slope widths were between 1.0 and 2.0. With an increase in the incident angle, the vertical amplification ratios were almost the same for each slope width.

Nonetheless, variations in the acceleration amplification ratios at the slope crest were complicated. The horizontal amplification ratios at the left crest first decreased and then increased with an increase in the incident angle (at slope widths of 2.0 and 4.0). The horizontal ratios first increased and then decreased as the incident angle increased (at slope widths of 0.5 and 1.0). In addition, the ratios increased from an incident angle of 5° to an incident angle of 20° at a slope width of 0.5, which could be interpreted by the superposition of the scattered waves in the narrow models. The vertical amplification ratios at the left crest first decreased and then increased with an increase in the angle of incidence. Furthermore, the horizontal amplification ratios at the right crest first increased and then decreased with an increase in the angle of incidence. The maximum horizontal ratios were obtained between 15° and 25° of the incident angle (at a slope width of 1.0). The vertical amplification ratios at the right crest were almost the same for various incident angles. The vertical ratios reached a maximum between 15° and 25° of the incident angles (at a slope width of 1.0). The above variations were in good agreement with the seismic responses of ground motions of PGA in Figure 21b, and these evolutions could be interpreted by the correlations between the wavelength and the slope widths.

In summary, the variations in the amplification ratios were mainly concentrated on the slope crest with varying angles of incidence, and these complexities were aggravated when the width was almost one wavelength.

4.3.3. Influence of Slope Inclination I

The inclination of the slope, which is defined as the width-depth ratio, varied from 0.5, 0.7, 1.0 and 1.5 to 2.0, whereas the other geometrical parameters (slope heights and slope widths) remained the same. The acceleration amplification ratios along the slope surface are illustrated in Figure 24 with varying angles of incidence.

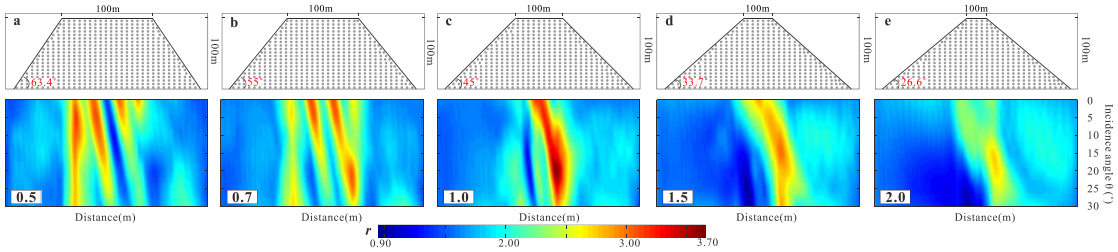

Figure 24. Variations of the seismic responses along the slope ridges and slope crests of the real amplification ratios (*r*) of PGA with varied angles of wave incidence at different slope inclinations. (**a**) slope inclination of 0.5, (**b**) slope inclination of 0.7, (**c**) slope inclination of 1.0 (**d**) slope inclination of 1.5 (**e**) slope inclination of 2.0.

In Figure 24, the acceleration amplification ratios moved from the left slope crest to the right slope crest when the slope model became gentle. The amplification ratios moved away from the wave source with an increase in the angles of incidence, especially in the gentle slope model. These evolutions are indicated by the scattered waves induced by slope inclinations. The ground motions reached a maximum when the incident angles fluctuated between 5° and 10° in the steep slope model ($i < 1.0$). However, the ground motions reached a maximum when the incident angles were between 15° and 20° in the gentle slope model ($i > 1.0$). Thus, the greater the slope inclinations, the closer the maximum acceleration amplification ratios were to the greater inclinations of the incident waves. In summary, the ground motions were mainly concentrated on the slope ridges. The oblique incident waves and slope inclinations changed the propagation of the seismic wave paths, and the scattered waves easily concentrated as the slope became gentle. The maximum acceleration amplification ratios were obtained in the oblique direction of the incident waves.

Similar to the analyses of the slope height and slope widths, the slope toe and slope crest are also presented with horizontal amplification ratios and vertical amplification ratios in Figures 25 and 26, respectively. The comprehensive relations between the incident angles and slope inclinations are discussed.

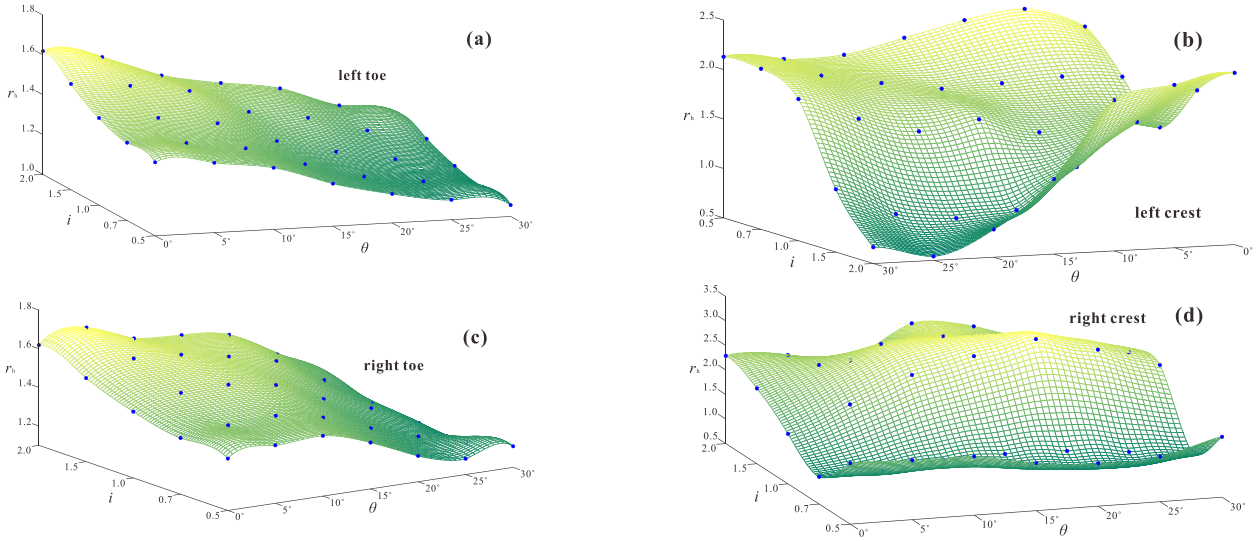

Figure 25. Variations of the horizontal amplification ratios (r_h) of PGA at the observation points ((**a**) left toe, (**b**) left crest, (**c**) right toe and (**d**) right crest) with varied angles of wave incidence at different slope inclinations.

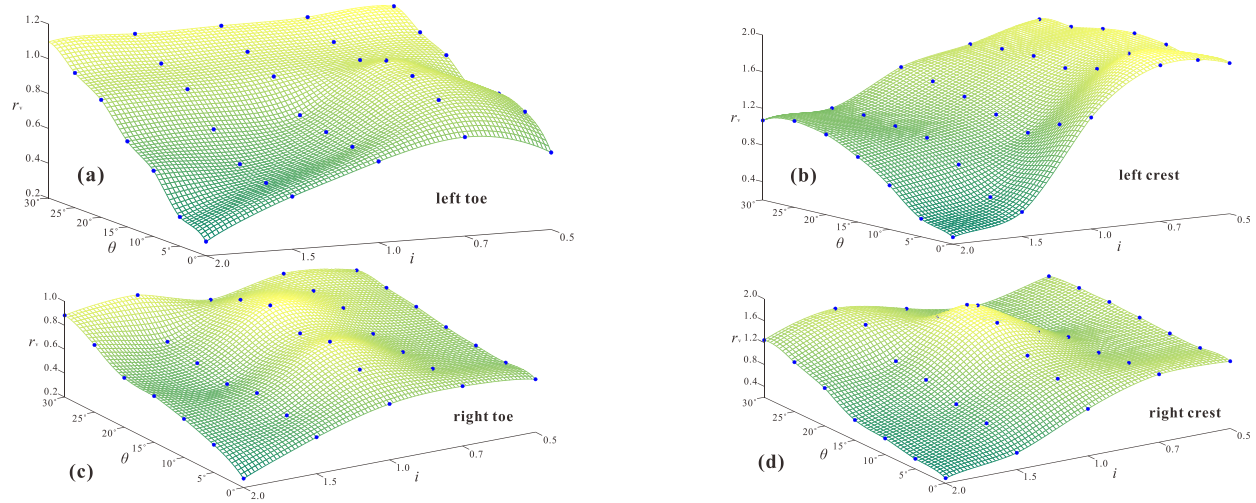

Figure 26. Variations of the vertical amplification ratios (r_v) of PGA at the observation points ((**a**) left toe, (**b**) left crest, (**c**) right toe and (**d**) right crest) with varied angles of wave incidence at different slope inclinations.

The horizontal amplification ratios of the slope toe monotonously decreased with an increase in the angle of incidence, whereas the horizontal ratios increased as the slope inclination increased. That is, the ground motions at the slope toe increased as the slope became gentle. However, the vertical amplification ratios of the slope toe increased monotonously with an increase in the angle of incidence, and the ratios gradually decreased when the slope became gentle.

The variations in the amplification ratios at the slope crest were complicated at varying incident angles. The horizontal amplification ratios at the left crest decreased with an increase in the angle of incidence, and the reduced amplitude intensified as the slope became steeper ($i < 1.0$). The horizontal amplification ratios at the right crest remained the same with an increase in the angle of incidence, and the maximum ratios fell between 1.0

and 1.5 of *i*. The vertical amplification ratios at the left crest and right crest decreased with an increase in slope inclination. The ratios were intensified at the left crest whereas they were alleviated at a slope inclination of 1.0, at an incident angle of 15°on the right crest.

In summary, the variations in the amplification ratios were concentrated on the slope crests at varying angles of incidence because the varying inclinations of slope ridges changed the propagation of wave paths in the topography.

5. Summary and Conclusions

In this study, ground motion amplification of the slope topography was analyzed using dynamic FEMs. The wave patterns, materials and slope sizes were discussed based on varying angles of incidence. A viscous-spring artificial boundary was borrowed, and an equivalent nodal force method was proposed to implement oblique incident waves in the FEM. Two numerical examples were adopted to verify the validity of the input method and the accuracy of the artificial boundary. Subsequently, the ground motions in slope topography were investigated with arbitrary directions of incidence, considering the main impact factors of site effects (wave patterns, materials and sizes of slope topography).

The main conclusions and findings are as follows: (1) the amplification effects are underestimated by the vertical incident waves, and the maximum ground motions are closely related to the scattered waves, which depend on the ridge inclinations and the incident directions. (2) Owing to the intense amplification effects under SV waves, the ground motions of slope topography are preferred for analysis using SV waves rather than P waves. (3) With an increase in the angles of incidence, the amplification effects are more complicated at the crest of the slope topography, and the amplification regions are focused on the ridges away from the epicenter. (4) The ground motion amplification effects are aggravated in soft materials owing to the much more scattered waves produced. The directions of the incident waves are a key factor in the analysis of ground motions in slope topography. The amplification effects of slope topography should be discussed separately owing to the complex transmission paths induced by oblique incident waves.

The results obtained here can be considered in the analysis of the ground motion amplification effects of slope topography subjected to earthquakes. The above findings were discussed in terms of three influencing factors that impact the topographic effects: the patterns of the incident waves, the materials of the slope and the slope sizes. The wave patterns that included P waves and SV waves were sufficient for the analysis of topographic effects. Even though the surface waves (e.g., Rayleigh and Love waves) have not been directly analyzed, they were still considered in this study because the conclusions were based on the incident body waves, that is, P waves or SV waves, and were actually a comprehensive result of body waves and surface waves. That is, the proposed input method can also express the impacts of Rayleigh waves (in two dimensions). Thus, the topographic effects calculated using P waves and SV waves in this study are meaningful and necessary. Even though the samples in the analysis of slope materials and slope sizes were relatively few, the conclusions could interpret several regularity phenomena, achieving the purpose of this study. Furthermore, the lack of experimental evidence for the comparison and calibration of the findings in the numerical studies is a serious obstacle [36,61]. Hence, a specific model should be established according to the study area while considering real materials based on the specific earthquake record for a specific study area. Data from field measurements should be collected simultaneously to support numerical modeling results.

Author Contributions: Conceptualization, C.Y.; methodology, C.Y. and W.-H.L.; software, C.Y.; validation, C.Y. and W.W.; formal analysis, C.Y. and W.-H.L.; writing—original draft preparation, C.Y. writing—review and editing, C.Y.; funding acquisition, C.Y. All authors have read and agreed to the published version of the manuscript.

Funding: This research was supported by the Postdoctoral Science Foundation of China (2021M692242); the National Natural Science Foundation of Hebei Province (E2021210072, E2021210036); and the Cen-

tral Leading Local Science and Technology Development Foundation of Hebei Province (216Z5403G). The support is gratefully acknowledged.

Institutional Review Board Statement: Not applicable.

Informed Consent Statement: Not applicable.

Data Availability Statement: Not applicable.

Conflicts of Interest: The authors declare no conflict of interest.

References

1. Alfaro, P.; Delgado, J.; García-Tortosa, F.J.; Lenti, L.; López, J.A.; López-Casado, C.; Martino, S. Widespread landslides induced by the Mw 5.1 earthquake of 11 May 2011 in Lorca, SE Spain. *Eng. Geol.* **2012**, *137-138*, 40–52. [CrossRef]
2. Collins, B.D.; Kayen, R.; Tanaka, Y. Spatial distribution of landslides triggered from the 2007 Niigata Chuetsu–Oki Japan Earthquake. *Eng. Geol.* **2012**, *127*, 14–26. [CrossRef]
3. Delgado, J.; García-Tortosa, F.J.; Garrido, J.; Loffredo, A.; López-Casado, C.; Martin-Rojas, I.; Rodríguez-Peces, M.J. Seismically-induced landslides by a low-magnitude earthquake: The M_w 4.7 Ossa De Montiel event (central Spain). *Eng. Geol.* **2015**, *196*, 280–285. [CrossRef]
4. Tang, C.; Ma, G.C.; Chang, M.; Li, W.L.; Zhang, D.D.; Jia, T.; Zhou, Z.Y. Landslides triggered by the 20 April 2013 Lushan earthquake, Sichuan Province, China. *Eng. Geol.* **2015**, *187*, 45–55. [CrossRef]
5. Wartman, J.; Dunham, L.; Tiwari, B.; Pradel, D. Landslides in eastern Honshu induced by the 2011 Tohoku earthquake. *Bull. Seism. Soc. Am.* **2013**, *103*, 1503–1521. [CrossRef]
6. Xu, C.; Xu, X.W.; Shyu, J.B.H. Database and spatial distribution of landslides triggered by the Lushan, China Mw 6.6 earthquake of 20 April 2013. *Geomorphology* **2015**, *248*, 77–92. [CrossRef]
7. Dunning, S.A.; Mitchell, W.A.; Rosser, N.J.; Petley, D.N. The Hattian Bala rock avalanche and associated landslides triggered by the Kashmir Earthquake of 8 October 2005. *Eng. Geol.* **2007**, *93*, 130–144. [CrossRef]
8. Owen, L.A.; Kamp, U.; Khattak, G.A.; Harp, E.L.; Keefer, D.K.; Bauer, M.A. Landslides triggered by the 8 October 2005 Kashmir earthquake. *Geomorphology* **2008**, *94*, 1–9. [CrossRef]
9. Yin, Y.P.; Wang, F.W.; Sun, P. Landslide hazards triggered by the 2008 Wenchuan earthquake, Sichuan, China. *Landslides* **2009**, *6*, 139–152. [CrossRef]
10. Huang, R.; Pei, X.; Fan, X.; Zhang, W.; Li, S.; Li, B. The characteristics and failure mechanism of the largest landslide triggered by the Wenchuan earthquake, May 12, 2008, China. *Landslides* **2011**, *9*, 131–142. [CrossRef]
11. Sepúlveda, S.A.; Murphy, W.; Jibson, R.W.; Petley, D.N. Seismically induced rock slope failures resulting from topographic amplification of strong ground motions: The case of Pacoima Canyon, California. *Eng. Geol.* **2005**, *80*, 336–348. [CrossRef]
12. Sepúlveda, S.A.; Murphy, W.; Petley, D.N. Topographic controls on coseismic rock slides during the 1999 Chi-Chi earthquake, Taiwan. *Q. J. Eng. Geol. Hydrogeol.* **2005**, *38*, 189–196. [CrossRef]
13. Bourdeau, C.; Havenith, H.B. Site effects modelling applied to the slope affected by the Suusamyr earthquake (Kyrgyzstan, 1992). *Eng. Geol.* **2008**, *97*, 126–145. [CrossRef]
14. Bozzano, F.; Lenti, L.; Martino, S.; Paciello, A.; Mugnozza, G.S. Self-excitation process due to local seismic amplification responsible for the reactivation of the Salcito landslide (Italy) on 31 October 2002. *J. Geophys. Res. Space Phys.* **2008**, *113*, 1–21. [CrossRef]
15. Del Gaudio, V.; Coccia, S.; Wasowski, J.; Gallipoli, M.R.; Mucciarelli, M. Detection of directivity in seismic site response from microtremor spectral analysis. *Nat. Hazards Earth Syst. Sci.* **2008**, *8*, 751–762. [CrossRef]
16. Bozzano, F.; Lenti, L.; Martino, S.; Paciello, A.; Mugnozza, G.S. Evidences of landslide earthquake triggering due to self-excitation process. *Int. J. Earth. Sci.* **2011**, *100*, 861–879. [CrossRef]
17. Lenti, L.; Martino, S. The interaction of seismic waves with step-like slopes and its influence on landslide movements. *Eng. Geol.* **2012**, *126*, 19–36. [CrossRef]
18. Athanasopoulos, G.A.; Pelekis, P.C.; Leonidou, E.A. Effects of surface topography on seismic ground response in the Egion (Greece) 15 June 1995 earthquake. *Soil. Dyn. Earthq. Eng.* **1999**, *18*, 135–149. [CrossRef]
19. Çelebi, M. Topographical and geological amplification: Case studies and engineering implications. *Struct. Saf.* **1991**, *10*, 199–217. [CrossRef]
20. Wang, W.; Liu, B.D.; Liu, X.; Yang, M.L.; Zhou, Z.H. Analysis on the hill topography effect based on the strong ground motion records of Wenchuan Ms8.0 earthquake. *Acta. Seismol. Sinica.* **2015**, *37*, 452–462.
21. Zaslavsky, Y.; Shapira, A. Experimental study of topographic amplification using the Israel seismic network. *J. Earthq. Eng.* **2000**, *4*, 43–65. [CrossRef]
22. Bakavoli, M.K.; Haghshenas, E. Experimental and numerical study of topographic site effect on a hill near Tehran. In Proceedings of 5th International Conference on Recent Advances in Geotechnical Earthquake Engineering and Soil Dynamics, San Diego, CA, USA, 24 May 2010; pp. 1–10.
23. Trifunac, M.D. Scattering of plane SH waves by a semi-cylindrical canyon. *Earthq. Eng. Struct. Dyn.* **1973**, *1*, 267–281. [CrossRef]

24. Wong, H.L.; Trifunac, M.D. Scattering of plane SH waves by a semi-elliptical canyon. *Earthq. Eng. Struct. Dyn.* **1974**, *3*, 157–169. [CrossRef]
25. Lee, V.W. Three-dimensional diffraction of plane P, SV & SH waves by a hemispherical alluvial valley. *Soil Dyn. Earthq. Eng.* **1984**, *3*, 133–144. [CrossRef]
26. Lee, V.W. Scattering of plane SH-waves by a semi-parabolic cylindrical canyon in an elastic half-space. *Geophys. J. Int.* **1990**, *100*, 79–86. [CrossRef]
27. Yuan, X.M.; Men, F.L. Scattering of plane SH waves by a semi-cylindrical hill. *Earthq. Eng. Struct. Dyn.* **1992**, *21*, 1091–1098. [CrossRef]
28. Du, X.L.; Xiong, J.G.; Guan, H.M. Boundary integration equation method to scattering of plane SH-waves. *Acta Seism. Sin.* **1993**, *6*, 609–618. [CrossRef]
29. Ashford, S.A.; Sitar, N. Analysis of topographic amplification of inclined shear waves in a steep coastal bluff. *Bull. Seismol. Soc. Am.* **1997**, *87*, 692–700. [CrossRef]
30. Ashford, S.A.; Sitar, N.; Lysmer, J.; Deng, N. Topographic effects on the seismic response of steep slopes. *Bull. Seism. Soc. Am.* **1997**, *87*, 701–709.
31. Han, F.; Wang, G.Z.; Kang, C.Y. Scattering of SH-waves on triangular hill joined by semi-cylindrical canyon. *Appl. Math. Mech.* **2011**, *32*, 309–326. [CrossRef]
32. Yang, Z.L.; Xu, H.N. Ground motion of two scalene triangle hills and a semi-cylindrical canyon under incident SH-waves. *Appl. Mech. Mater.* **2012**, *21–126*, 862–866. [CrossRef]
33. Lee, V.W.; Liu, W.Y. Two-dimensional scattering and diffraction of P- and SV-waves around a semi-circular canyon in an elastic half-space: An analytic solution via a stress-free wave function. *Soil Dyn. Earthq. Eng.* **2014**, *63*, 110–119. [CrossRef]
34. Zhang, N.; Gao, Y.F.; Pak, R.Y.S. Soil and topographic effects on ground motion of a surficially inhomogeneous semi-cylindrical canyon under oblique incident SH waves. *Soil. Dyn. Earthq. Eng.* **2017**, *95*, 17–28. [CrossRef]
35. Meunier, P.; Hovius, N.; Haines, J.A. Topographic site effects and the location of earthquake induced landslides. *Earth Planet. Sci. Lett.* **2008**, *275*, 221–232. [CrossRef]
36. Bouckovalas, G.D.; Papadimitriou, A.G. Numerical evaluation of slope topography effects on seismic ground motion. *Soil Dyn. Earthq. Eng.* **2005**, *25*, 547–558. [CrossRef]
37. Pagliaroli, A.; Lanzo, G.; Beniamino, E. Numerical evaluation of topographic effects at the nicastro ridge in Southern Italy. *J. Earthq. Eng.* **2011**, *15*, 404–432. [CrossRef]
38. Narayan, J.P.; Kumar, V. Study of combined effects of sediment rheology and basement focusing in an unbounded viscoelastic medium using P-SV-Wave finite-difference modeling. *Acta Geophys.* **2014**, *62*, 1214–1245. [CrossRef]
39. Hailemikael, S.; Lenti, L.; Martino, S.; Paciello, A.; Rossi, D.; Mugnozza, G.S. Ground-motion amplification at the Colle di Roio ridge, Central Italy: A combined effect of stratigraphy and topography. *Geophys. J. Int.* **2016**, *206*, 1–18. [CrossRef]
40. Assimaki, D.; Gazetas, G.; Kausel, E. Effects of local soil conditions on the topographic aggravation of seismic motion: Parametric investigation and recorded field evidence from the 1999 Athens earthquake. *Bull. Seism. Soc. Am.* **2005**, *95*, 1059–1089. [CrossRef]
41. Assimaki, D.; Kausel, E.; Gazetas, G. Wave propagation and soil structure interaction on a cliff crest during the 1999 Athens earthquake. *Soil. Dyn. Earthq. Eng.* **2005**, *25*, 513–527. [CrossRef]
42. Lo Presti, D.C.F.; Lai, C.; Puci, I. ONDA: Computer code for nonlinear seismic response analyses of soil deposits. *J. Geotech. Geoenviron. Eng.* **2006**, *132*, 223–235. [CrossRef]
43. Di Fiore, V. Seismic site amplification induced by topographic irregularity: Results of a numerical analysis on 2D synthetic models. *Eng. Geol.* **2010**, *114*, 109–115. [CrossRef]
44. Tripe, R.; Kontoe, S.; Wong, T.K.C. Slope topography effects on ground motion in the presence of deep soil layers. *Soil Dyn. Earthq. Eng.* **2013**, *50*, 72–84. [CrossRef]
45. Rizzitano, S.; Cascone, E.; Biondi, G. Coupling of topographic and stratigraphic effects on seismic response of slopes through 2D linear and equivalent linear analyses. *Soil Dyn. Earthq. Eng.* **2014**, *67*, 66–84. [CrossRef]
46. Nguyen, K.V.; Gatmiri, B. Evaluation of seismic ground motion induced by topographic irregularity. *Soil Dyn. Earthq. Eng.* **2007**, *27*, 183–188. [CrossRef]
47. Pagliaroli, A.; Avalle, A.; Falcucci, E.; Gori, S.; Galadini, F. Numerical and experimental evaluation of site effects at ridges characterized by complex geological setting. *Bull. Earthq. Eng.* **2015**, *13*, 2841–2865. [CrossRef]
48. Gischig, V.S.; Eberhardt, E.; Moore, J.R.; Hungr, O. On the seismic response of deep-seated rock slope instabilities—Insights from numerical modeling. *Eng. Geol.* **2015**, *193*, 1–18. [CrossRef]
49. Narayan, J.P.; Kumar, V. A numerical study of effects of ridge-weathering and ridge-shape-ratio on the ground motion characteristics. *J. Seism.* **2015**, *19*, 83–104. [CrossRef]
50. Li, H.; Liu, Y.; Liu, L.; Liu, B.; Xia, X. Numerical evaluation of topographic effects on seismic response of single-faced rock slopes. *Bull. Int. Assoc. Eng. Geol. Environ.* **2017**, 1873–1891. [CrossRef]
51. Jin, X.; Liao, Z.P. Statistical research on S-wave incident angle. *Earthq. Resear. Chin.* **1994**, *8*, 121–131.
52. Takahiro, S.; Kazuhiko, K.; Yoichi, S.; Dai, K.; Toru, M.; Ryoichi, T.; Chiaki, Y.; Takeshi, U. Estimation of earthquake motion incident angle at rock site. In Proceedings of the 12th World Conference Earthquake Engineering, NZ National Society for Earthquake Engineering, Auckland, New Zealand, 16 April 2000; pp. 1–8.

53. Kuhlemeyer, R.L.; Lysmer, J. Finite element method accuracy for wave propagation problems. *J. Soil Mech. Found. Div.* **1973**, *99*, 421–427. [CrossRef]
54. Deeks, A.J.; Randolph, M.F. Axisymmetric time-domain transmitting boundaries. *J. Eng. Mech.* **1994**, *120*, 25–42. [CrossRef]
55. Liu, J.B.; Lv, Y.D. A direct method for analysis of dynamic soil-structure interaction based on interface idea. *Chin. Civ. Eng. J.* **1998**, *83*, 261–276. [CrossRef]
56. Du, X.L.; Zhao, M.; Wang, J.T. A stress artificial boundary in FEA for near-field wave problem. *Chin. J. Theor. Appl. Mech.* **2006**, *38*, 49–56.
57. Yin, C.; Li, W.H.; Zhao, C.G.; Kong, X.A. Impact of tensile strength and incident angles on a soil slope under earthquake SV-waves. *Eng. Geol.* **2019**, *260*, 1–11. [CrossRef]
58. Eringen, A.C.; Suhubi, E.S. *Elastodynamics*; Academic Press: New York, NY, USA, 1975.
59. Ewing, W.M.; Jardetzky, W.S.; Press, F.; Beiser, A. *Elastic Waves in Layered Media*; McGraw-Hill: New York, NY, USA, 1957.
60. Wong, H.L. Effect of surface topography on the diffraction of P, SV, and Rayleigh waves. *Bull. Seismol. Soc. Am.* **1982**, *72*, 1167–1183.
61. Lenti, L.; Martino, S. A parametric numerical study of the interaction between seismic waves and *Landslides* for the evaluation of the susceptibility to seismically induced displacements. *Bull. Seismol. Soc. Am.* **2013**, *103*, 33–56. [CrossRef]